http://dx.doi.org/10.1016/j.ijplas.2015.08.003

Modeling of slip, twinning and transformation induced plastic deformation for TWIP steel based on crystal plasticity

C.Y. Sun*[a], N. Guo[a], M.W. Fu[b], S.W. Wang[a],

[a] School of mechanical engineering, University of Science and Technology Beijing, Beijing, 100083, China

[b] Department of Mechanical Engineering, The Hong Kong Polytechnic University, Hung Hom, Kowloon, Hong Kong

Abstract

One of the most critical issues in development of micromechanics models for TWIP steel is to establish the continuum constitutive model which can accurately represent and model the characteristic plastic deformation at macro level. However, the uncertainty in describing the evolution of deformation state variables based on crystal plasticity theory poses a great challenge in handling the complex plasticity deformation with different deformation mechanisms and their complicated interactions and interplays at microscopic scale and thus becomes a non-trivial issue. Many attempts to address this issue by coupling slip and twinning or slip and transformation have been proven to be efficient via comparing and corroborating the predicted texture evolution using crystal plasticity theory with experiments. An accurate constitutive model, however, needs to be established to articulate and model the interactions of slip, twinning and transformation, which have been observed in experiments. In this paper, a micromechanics model for modeling of slip, twinning and transformation induced plasticity deformation of twinning-induced plasticity (TWIP) steel is proposed by using the crystal plasticity approach. The model serves as a feasible approach to reflecting the micro deformation mechanisms during the plastic deformation process of TWIP crystals. The phase transformation is introduced and represented by the classic elasto-plastic constitutive model. The algorithms for realization of the developed model are implemented in

ABAQUS/Standard platform using UMAT. Furthermore, different deformation mechanisms of the microscopic plastic deformation modes of TWIP single crystals are analyzed based on the proposed models. The simulation results by using the developed model reveals that both twinning and transformation have an obvious effect on hardening and transformation, which cause the decrease of stress of single crystal, and the sequence of transformation and twinning rotation can be determined according to the proposed model.

Keywords: Phase transformation; Twinning; Crystal plasticity; Polycrystalline material; Numerical algorithms

*The Corresponding author: C.Y. Sun.

Tel.: +86 10 62334197, Fax: +86 10 62329145.

E-mail: suncy@ustb.edu.cn.

1. Introduction

The development of advanced steels with high strength, good ductility and toughness has long been an eluded and tantalized issue. Typical high strength steels including dual phase, TRIP and boron steels have been widely used in automobile industry. Recently, another concept of advanced steel has gained a great deal of attention driven by the weight reduction of vehicle, viz., development of low stacking fault energy (SFE) austenitic high Mn steels showing twinning-induced plasticity (TWIP) effect. The so-called TWIP steels exhibit not only high tensile strength (600-1100 MPa), admirable ductility (60-95%), but also excellent plasticity, toughness and formability. Especially, the product of strength and elongation could be up to 50000 MPa· %, which is four to five times the traditional **IF** steel and martensitic steel, and at least two times the dual phase steel (Lee, W. et al., 2009; Sung et al., 2010; Kadkhodapour, J., et al., 2011; Carvalho, T. et al., 2013; Sun and Wagoner, 2013) and TRIP steel (Mohr, D. et al, 2010; Lee et al., 2010; Fischlschweiger et al., 2012). These excellent mechanical properties are related to the occurrence of competitive and different deformation modes, viz., crystallographic slip, mechanical twinning and martensitic phase transformation (Shiekhelsouk et al., 2009).

In order to reveal the mechanism of the high strength plasticity product induced by coupling different plastic deformation modes, a large number of experiments focused on microstructure evolution of TWIP steel before and after plastic deformation had been conducted by employing modern microscopic detection technologies, including SEM, XRD, TEM, Electron Backscattered Scattering Detection (EBSD), et al. and attempting to explore the different deformation mechanisms (Mi et al.,2005; Barbier et al.,2009; Jin et al., 2009; Liang et al., 2009; Sabet et al., 2009; Dini et al., 2010; Jiménez et al., 2010; Gutierrez et al., 2012a). The coupling of dislocation slip and twinning induced plasticity has been considered as a predominantly microscopic deformation mechanism for the low stack fault energy FCC

materials. In order to reveal and dissect the deformation mechanism induced by slip and twinning, which are competing and cooperating with each other, Barbier et al. (2009) performed a tensile test of TWIP steel (Fe–22Mn–0.6C) with the average grain size of 2.6 um at room temperature, and further analyzed the microstructure and the texture <111>//TD fiber, <100>//TD fiber (parallel to TD direction) by using EBSD. The experiments showed that the strong interaction among crystallographic slip, mechanical twinning and texture components is described and discussed for the tensile test along tensile direction. In addition, Jiménez et al. (2010) corroborated that the governing mechanism of TWIP single grain depends on its crystallographic orientation relative to tensile direction. Furthermore, Saleh et al. (2013) explained the activation of twinning systems with respect to the evolution of dislocation slip and described the evolution of lattice strain during the cyclic loading of low stacking fault energy materials deformed via concurrent slip and twinning. Particularly, a lot of efforts (Vercammen et al., 2004; Yang et al., 2006; Jin et al., 2009; Sabet et al., 2009; Sevillano et al., 2009; Dini et al., 2010; Gutierrez-Urrutia et al., 2012b; Yang et al. 2013) have been provided to explain the phenomenon that twinning increases strain hardening. Furthermore, Idrissi et al. (2010) took an efficient step to reveal the mechanism of twinning nucleation and propagation by Transmission Electron Microscope (TEM). With an attempt to explore the micro plastic deformation mechanisms of TWIP steel gradually, martensite variant was observed during the deformation process at low temperature in the previous experiments, showing the deformation mechanism of slip and transformation (Mi et al., 2005; Huang et al., 2006; Liang et al., 2009; Yang et al., 2010; Koyama et al., 2011; Wu et al., 2012).

Furthermore, qualitative analysis has been done to explain the reason why slip and transformation, and twinning and transformation could induce plasticity (Koyama et al. 2011). It indicates that there is also a plastic deformation mechanism, viz., transformation-coupling

with slip or twinning (TRIP/TWIP effect) at a certain condition, which could enhance the mechanical properties of TWIP steel. These studies reveal that the contribution to the macroscopic plastic deformation is determined by the coupling different mechanisms, and also provide a basis for the theoretical modeling of slip coupling twinning and transformation. However, it is difficult, if not impossible, to observe the evolution process of slip, twinning and transformation systems simultaneously. The experiments with the aim at explanation for microscopic deformation mechanisms by coupling slip, twinning and transformation would have a limited capacity in describing the microscopic evolution due to the lack of efficient and available experimental techniques.

From the theoretical point of view, most models intend to reveal the effect of different microscopic mechanisms on the macroscopically plastic deformation of high symmetrical FCC crystal essentially. To explore the mechanism of twinning induced plasticity, many researchers attempted to establish different kinds of models. Among these models which emphasize the analysis of strain hardening and texture evolution of deformation twinning at the grain scale, they are mathematically based models (Kalidindi, 1998; Staroselsky and Anand, 2003) or physically based ones for the strain hardening and texture evolution (Bouaziz and Guelton, 2001; Perlade et al., 2003; Allain et al.,2004; Bouaziz et al., 2008; Shiekhelsouk et al., 2009; Barbier et al., 2012; Bouaziz, 2012; Gao and Zhang, 2012; Knezevic, M. et al., 2014). Particularly, the research done by Knezevic et al. (2013a) is focused on the establishment of a polycrystalline plasticity model of the hexagonal metals, but it is also useful for investigation of the strain hardening of FCC type metals. In this research, a previously developed strain rate- and temperature-sensitive hardening law is extended, which explicitly accounts for the evolution of dislocation densities by including the effects of reverse dislocation motion and de-twinning and applied to any metal deformation by slip and twinning. In the previous work of the authors, based on the evolution of

dislocation density and the twin volume fraction, a physically based constitutive model of Fe-22Mn-0.6C TWIP steel was developed by taking into account the influence of slip inside the twin on plastic deformation and the difference of the average Taylor factors between the twinned regions and matrix regions (Sun et al. 2014). The physical models based on dislocation density evolution describe the relationship between twinning and dislocation density and the contribution to twinning on macroscopic plasticity. Recently, a number of models have been proposed (Brown et al., 2012, Capolungo et al., 2009, Oppedal et al., 2012) considering slip and twinning interactions that allow the hardening by different slip and twinning modes to have their own evolution for HCP type metals. These physical models show their unique characteristics in representing the evolution of slip and twinning systems, also in articulating the influence of deformation twins on slip evolution. To articulate the effect of the transformation on the material mechanical properties, many researchers (Levitas, 2002; Suiker and Turteltaub, 2005; Turteltaub and Suiker, 2005; Tjahjanto et al., 2008a; Tjahjanto et al., 2008b) have established thermodynamic models based on a large deformation to reveal the thermal condition for the onset of transformation and the evolution of transformation volume fraction. Particularly, Turteltaub et al. (2005) established the martensitic phase transformation microscopic mechanical model based on the crystal plasticity formulation suitable for TRIP steel by analyzing the martensitic phase transformation from cubic lattice to square lattice. However, it is also difficult for the models mentioned above to represent the influence of transformation on slip and twinning.

Recently, based on the crystal plasticity (CP) approach, a series of plastic deformation constitutive models of TWIP steel coupling slip and twinning were developed and the twinning volume fraction and its saturated value were introduced to consider the effect of twinning on hardening and slip, respectively (Kalidindi, 1998; Salem et al., 2005; Staroselsky and Anand, 2003). Meanwhile, many researches (Manchiraju and Anderson, 2010; Tjahjanto

et al., 2008a, b; Turteltaub and Suiker; 2005; Levitas, 2002) proposed to consider the transformation in the constitutive model using the same principle. These models can represent the texture evolution well, however, in specific conditions, the change of martensite can be observed during the plastic deformation of TWIP steel, which indicates that transformation would make contribution to the plastic deformation at macro level. Therefore, the combined model considering slip, twinning and transformation will be more comprehensive and efficient in reflecting the macroscopic deformation of TWIP materials.

However, the challenge is critical in describing the onset of different mechanisms in introducing the transformation into the model considering slip and twinning, and modeling the evolution of slip, twinning and transformation, respectively. To address this issue, a micromechanics model representing slip, twinning and transformation induced plasticity for TWIP steel based on crystal plasticity is established in this paper.

In this paper, the micromechanics explanation based on the three deformation mechanisms (slip, twinning, transformation) are represented and the dynamic and kinematic description of the proposed model is discussed with respect to continuum mechanics. The improvement of crystal plasticity framework is highlighted according to the previous models (Kalidindi, 1998; Salem et al., 2005; Staroselsky and Anand, 2003), while the constitutive relationship of TWIP steel single crystal is represented in the elasto-plastic domain. The updates of state variables are particularly described and a user material subroutine (UMAT) is developed for realizing the presented constitutive relationship of TWIP crystals in ABAQUS/Standard. Finally, the parameters are calibrated based on the prior researches (Salem et al., 2005; Kalidindi, 1998; Suiker and Turteltaub, 2005). Furthermore, case study examples are provided to verify the efficiency of the developed model in terms of reflecting the deformation mechanisms of single crystal.

2. Constitutive model considering slip, twinning and transformation mechanisms

2.1 Micro-deformation mechanisms of TWIP steel

Plastic slip occurs when one part of the crystal slides over another takes advantage of the periodic nature of crystals. Since the resistance to this sliding is very high, slip happens through the motion of dislocations. Typically slip is restricted to a few (symmetry-related) slip systems consisting of a slip plane and a slip direction, and slip generally occurs when the local stress projected to the plane exceeds a critical value, as shown in Fig.1 (a). The basic deformation schematic of twinning is illustrated in Fig. 1 (b). In order to verify the reliability of the twinning promoted by partial dislocation, Godet et al. (2006) demonstrated that the Schmid factor could be used to estimate the onset of twin systems. Most models depend on a simple deterministic critical resolved shear stress (CRSS) based law for describing nucleation and subsequent propagation of twins (Salem et al., 2005; Abdolvand et al., 2011).

A more detailed explanation of twin deformation mechanisms, including twin nucleation, twin growth, twin shrinkage and re-twinning, is proposed by Wang et al. (2013) via establishing a new crystal plasticity model, considering the twinning and de-twinning of the HCP style materials. Moreover, the twin nucleation and twin growth are associated with deformation twinning, and twin shrinkage and re-twinning are associated with de-twinning. In addition to the internal dislocation mechanism, another critical factor of twin deformation mechanism is the determination of Schmid factor. Abdolvand, H. et al (2011) gave an explicit description of the twin and child twin, using the different Schmid factor, respectively, meanwhile, the twin volume fraction with respect to the twinning deformation mechanisms is also distinguished according to the different regions. Recently, a stochastic model for the nucleation of deformation twins in HCP polycrystals was presented by Niezgoda et al. (2014). Twin nucleation is modeled through its dependence on the smaller length scale material and mechanical details, which enables this new approach to be able to model twin nucleation

except the critical resolved shear stress (CRSS). In this research, the CRSS value for determination of the twin nucleation is also used since one of the focuses of this research is on the combination of slip, twinning and transformation, instead of the twin nucleation. But it is necessary to introduce more suitable approaches in determination of the twin nucleation in future study.

Being considered as a shear deformation mechanism, martensitic transformation is driven by shearing and causes an embossed effect on the surfaces of steels, which is indicated in Fig. 1(c). In terms of crystalline structure, martensite has a body-centered tetragonal (BCT) lattice (α-martensite) and a hexagonal close packed (HCP) lattice (ε-martensite). Koyama et al. (2011) concluded that ε-martensite is a dominant type when martensite transformation occurs in Fe–17Mn–0.6C TWIP steel, which significantly affects the orientation change in austenite-martensite transformation during the tensile deformation. It is thus necessary to model the ε-martensite transformation. It is well known that ε-martensite and α-martensite are stress-assisted and strain-induced martensitic transformations, respectively. In this paper, the transformation model presented by Turteltaub (2005) is introduced into the framework considering slip, twinning and transformation using crystal plasticity approach since it is intended for stress-assisted martensitic transformation. Furthermore, according to the crystallography and dynamics of martensitic transformation, the driving force derived from the Helmholtz free energy per unit is introduced into the proposed model as the criterion to estimate the activation of transformation (Manchiraju and Anderson, 2010). The details of the ε-martensite transformation model are described in Section 2.2.

There are two aspects of effects to be considered in crystal plasticity theory. One is the plastic deformation mechanism; the other is the rigid rotation of lattice (Li et al, 2008). The schematic of rotation during the tensile test is illustrated in Fig. 1(d), in which the tension process of an idealized single crystal with one active slip system is presented to show the

nature of lattice rotation.

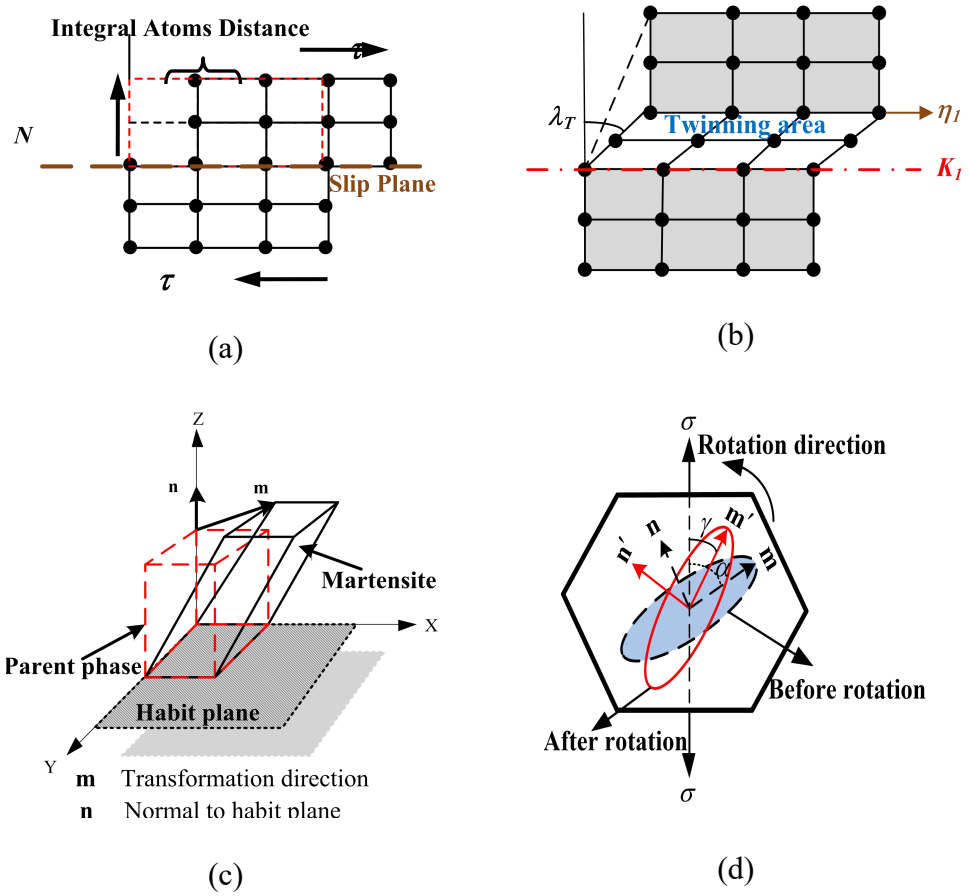

Fig.1. Schematic of different micro-deformation mechanisms. (a) Production of slip deformation by a homogeneous shear. Atoms move along the slip plane under the shear stress τ and N stands for the normal to the slip plane. (b) Schematic of twin shear deformation. λ_T denotes the twinning shear and the dashed line indicates the average shear of the material volume. (c) The parent phase (red dashed line) translates to martensite (black solid line) under the effect of shear deformation; the **m** and **n** indicate the transformation direction and the normal to habit plane, respectively. (d) Crystal rotation during the process of uniaxial tensile; the α and γ denote the amount of shear with respect to the status before rotation and after rotation, respectively.

2.2 Improvement of crystal plasticity framework

The main physical mechanism of crystal plastic deformation at ambient temperatures is

considered as the flow of dislocations along crystal slip systems. In crystal plasticity theory, massive dislocations on slip systems are represented in a continuum sense as a plastic shear strain γ. So, crystal plasticity is considered to be a physically based theory (Li et al., 2008). Following the work of Kalidindi et al. (1992), the decomposition of the deformation gradient tensor, $\mathbf{F}$, as shown in Fig.2., is formulated as

$$\mathbf{F} = \mathbf{F}^e \cdot \mathbf{F}^p \tag{1}$$

where $\mathbf{F}^e$ is the "elastic" deformation and the deformation component due to the reversible response of the lattice to external load and displacement, as well as rigid-body rotation, while $\mathbf{F}^p$ is the "plastic" deformation and an irreversible permanent deformation that persists when all the external forces and displacements that produce the deformation are removed.

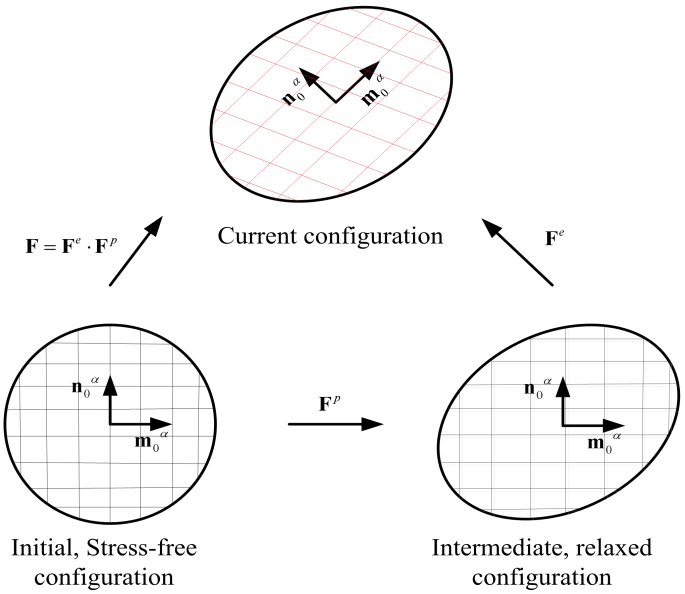

Fig.2. The schematic representation of the classic decomposition of deformation gradient **F**, which is divided into the elastic and plastic parts.

In addition, it is necessary to describe the rate dependent deformation gradient for explaining the evolution of finite deformation kinematics. The velocity of each material point of a body

in motion forms a vector field measured in the current configuration. The spatial gradient of the total velocity is obtained as:

$$\mathbf{L} = \dot{\mathbf{F}} \cdot \mathbf{F}^{-1} = \dot{\mathbf{F}}^{e} \cdot \mathbf{F}^{e^{-1}} + \dot{\mathbf{F}}^{e} \cdot \dot{\mathbf{F}}^{p} \cdot \mathbf{F}^{p^{-1}} \cdot \mathbf{F}^{e^{-1}} = \mathbf{L}^{e} + \mathbf{L}^{p} \tag{2}$$

where $\mathbf{L}^{e}$ is the velocity gradient in the current configuration relative to the plastic configuration, and $\mathbf{L}^{p}$ is the spatial velocity gradient in plastic configuration relative to the reference configuration.

For metallic materials, the elastic stretch of single crystal is small. Hence, the constitutive equation for stress could be linear with the following format:

$$\mathbf{T}^{e} = \mathfrak{R} : \mathbf{E}^{e} \tag{3}$$

where $\mathfrak{R}$ is a fourth-order anisotropic elasticity tensor; $\mathbf{E}^{e}$ and $\mathbf{T}^{e}$ are Green elastic strain measure and the symmetric second Piola-Kirchoff stress measure relative to the relaxed configuration, respectively. These measures are defined in the following equations. The elastic strain measure is defined as:

$$\mathbf{E}^{e} = \frac{1}{2}(\mathbf{F}^{e^{\mathrm{T}}} \cdot \mathbf{F}^{e} - \mathbf{I}) \tag{4}$$

where $\mathbf{C}$ is the elastic right Cauchy-Green tensor, defined as:

$$\mathbf{C} = (\mathbf{F}^{e})^{\mathrm{T}} \cdot \mathbf{F}^{e} \tag{5}$$

On the other hand, the stress measure, $\mathbf{T}^{e}$, which is the work conjugate to the employed strain measure, is designated as:

$$\mathbf{T}^{e} = \mathbf{F}^{e^{-1}} \cdot \left\{ \det(\mathbf{F}^{e}) \cdot \boldsymbol{\sigma} \right\} \cdot \mathbf{F}^{e^{-\mathrm{T}}} \tag{6}$$

For the deformation due to simple dislocation slip, the plastic velocity gradient is the sum of the shearing rate on each active slip system, and thus

$$\mathbf{L}_{\mathrm{p}} = \sum_{\alpha=1}^{n} \dot{\gamma}^{\alpha} \mathbf{m}^{\alpha} \otimes \mathbf{n}^{\alpha} \tag{7}$$

where $\dot{\gamma}^{\alpha}$ is the scalar shearing rate associated with the α slip system, $\mathbf{m}^{\alpha}$ is a unit

vector in the direction of the slip, and $\mathbf{n}^{\alpha}$ is the unit normal to the plane of the slip, and n is the number of slip systems. In addition, $\mathbf{m}^{\alpha}$ and $\mathbf{n}^{\alpha}$ are defined in the reference configuration, and $\mathbf{m}^{\alpha} \cdot \mathbf{n}^{\alpha} = 0$, so that the slip is a simple shear.

The resolved shear stress τ^{α} associated with the α slip system is defined as follows:

$$\tau^{\alpha} = \boldsymbol{\sigma} : \mathbf{S}^{\alpha} \tag{8}$$

The slip system will be active when the value of τ is greater than the critical value τ^{c}. Although strain-induced twinning has been investigated for years (Christian and Mahajan, 1995), most of its governing physical mechanisms still remain unclear. Numerous studies have aimed at identifying the influence of the deformation conditions and material properties on deformation twinning, focusing on temperature, grain size and stacking fault energy and their respective influence on twin nucleation and growth. Some references are listed in Table 1 corresponding to various kinds of factors on deformation twinning. Except for the factors given, chemical component, strain conditions and precipitate have an impact on twinning.

Table 1. References for different factors on deformation twinning.

Main factors	Reference
Temperature, strain rate	Galindo-Nava et al.(2014), Knezevic et al. (2013a), Knezevic et al. (2013b), Hokka et al.(2006), Piao et al. (2012), Brown et al. (2012), Li et al. (2010), Oberson and Ankem (2009)
Grain size	Gutierrez-Urrutia, et al.(2012b), Duhamel et al. (2010)
Stacking fault energy	Shiekhelsouk et al (2009), Beyerlein et al (2011)

Doquet (1993) brought the phenomenological description of twinning into the framework of crystal plasticity finite element analysis in the early years, then the corresponding

implementation into a FE scheme was proposed by Kalidindi (1998, 2001) and further developed in Kalidindi (2004). A mechanical twin formally corresponds to a sheared volume for which the lattice orientation is transformed into its mirror image across a so-called twin plane. A vector of the initial lattice is moved into its new position in the twin through a rotation matrix **Q**. Note that $\mathbf{L}^{\mathrm{mt}}$ and $\mathbf{L}^{\mathrm{tw}}$ can be related to each other by a coordinate transformation law as

$$\mathbf{L}^{tw} = \mathbf{L}^{mt} \cdot \mathbf{Q},\ \mathbf{Q} = 2\mathbf{n} \otimes \mathbf{n} - \delta_{ij} \tag{9}$$

where $\mathbf{n}$ is the twin plane unit normal and δ_{ij} is Kronecker's symbol.

Kalidindi (1998) proposed that the Cauchy stress in the crystal ($\boldsymbol{\sigma}$) is assumed to be given by the volume average of the stresses in the matrix and the twinned regions as

$$\boldsymbol{\sigma} = (1.0 - \sum_{\alpha} f^{\alpha})\boldsymbol{\sigma}^{mt} + \sum_{\alpha} f^{\alpha}\boldsymbol{\sigma}^{tw\alpha} \tag{10}$$

where f^{α} denotes the volume fraction of the grain that has been twinned to the α-twin system, and $\boldsymbol{\sigma}^{tw\alpha}$ is the Cauchy stress in the α-twinned region.

The description of transformation model could be divided into two scales: 1) macroscopic and 2) mesoscopic. The phenomenological approach is used for both of them. In this paper, the focus is on the mesoscopic description of ε-transformation. For the non-thermal elastic martensitic transformation, many researchers (Turteltaub et al., 2005; Cherkaoui et al., 2000; Fischer et al., 2005; Levitas et al, 2009) have attempted to establish a thermomechanical description at mesoscopic scale. Particularly, Turteltaub et al. (2005) have made a further step that the thermomechanical model of transformation was formulated in the CP framework.

Turteltaub et al. (2005) proposed that the deformation gradient associated with the transformation dynamics is denoted as:

$$\mathbf{F} = \mathbf{F}^{e} \cdot \mathbf{F}^{tr} \tag{11}$$

$$\mathbf{F}^{tr} = \mathbf{I} + \sum_{i=1}^{M} \xi^{(i)} \mathbf{b}^i \otimes \mathbf{d}^i \tag{12}$$

where vectors $\mathbf{b}^i$ and $\mathbf{d}^i$ are, respectively, the transformation shape strain vector and the normal to the habit plane of the transformation system i (measured in the reference configuration), $\mathbf{I}$ is the second-order identity tensor and $\xi^{(i)}$ is the martensitic volume fraction of i^{th} system.

The stress power $\mathbf{P} \cdot \dot{\mathbf{F}}$ is obtained by time derivative of Eqs. (11) and (12):

$$\mathbf{P} \cdot \dot{\mathbf{F}} = (\mathbf{P} \cdot \mathbf{F}_{tr}^{T}) \cdot \dot{\mathbf{F}}^{e} + \sum_{\alpha=1}^{M} \tau_m^{(\alpha)} \dot{\xi}^{(\alpha)} \tag{13}$$

where $\dot{\xi}^{(\alpha)}$ is the rate of change of the martensitic volume fraction of transformation system α and $\tau_m^{(\alpha)}$ is the corresponding resolved stress for transformation, given by

$$\tau_m^{(\alpha)} = \left(\mathbf{F}^{e^{\mathrm{T}}} \cdot \mathbf{P} \right) \cdot \left(\mathbf{b}^{(\alpha)} \otimes \mathbf{d}^{(\alpha)} \right) \tag{14}$$

The driving force for the phase transformation, denoted as f^i, can be written as:

$$f^i = f_m^i + f_{th}^i + f_d^i + f_s^i \tag{15}$$

where f_m^i, f_{th}^i, f_d^i and f_s^i represent the mechanical, thermal, defect and surface energy contributions to the transformation driving force, respectively.

The transformation rate is viewed as sufficiently fast to ensure that the energetic driving force f_t, which forms the plate type t, is always bounded by a critical value f_c,

$$-f_c \le f_t \left(\nu_t, \boldsymbol{\sigma}, \theta \right) \le f_c \tag{16}$$

Thus, if the Cauchy stress $\boldsymbol{\sigma}$ or temperature are incremented so as to make $| f_t | > f_c$, the volume fraction ν_t instantly changes via the forward or reverse austenite martensite transformation to ensure the consistency condition $| f_t | = f_c$. When f_t is within the bounds, ν_t does not change.

The energetic driving force to increase volume fraction ν_t is

$$f_t = \mathbf{b}_t^{Trans} \cdot (\mathbf{F}^e \cdot \boldsymbol{\sigma} \cdot \mathbf{F}^e \cdot \boldsymbol{\sigma}) \cdot \mathbf{m}_t^{Trans} - \frac{\lambda_T}{\theta_T}\left(\theta - \theta_T\right) - \sum_{u=1}^{N_T} h_{tu}\nu_u \tag{17}$$

where $\mathbf{b}_t^{Trans}$ and $\mathbf{m}_t^{Trans}$ stand for the normal vector and the direction vector of transformation, respectively. The first term at the right side is the transformation shear stress τ^{Trans}. In addition, λ_T and θ_T act as the latent heat of transformation per unit volume and the equilibrium transformation temperature, respectively. Furthermore, the hardening modulus h_{tu} between different transformation systems is considered as a non-effect item due to its difficulty in describing the hardening law.

To reveal the onset and evolution of transformation, there is a need to look into the nucleation of martensite, which is determined by the critical internal energy that is the threshold energy the austenite martensite transformation needs. The critical internal energy contains the contribution to nucleation of new interface, the remaining contributions, which are not explicitly quantified, are collectively represented as a critical threshold value f_{cr}^i for the driving force. Therefore, the critical condition of the onset of martensite transformation can be expressed as:

$$f^i = f_{cr}^i \tag{18}$$

From the standpoint of crystallography, martensite phase transformation is irreversible during the unloading process for TWIP steel. As a consequence, it is necessary to take the irreversibility into account in modelling of the martensite evolution of TWIP steel. Turteltaub (2005) presented an ideal and easy-to-implement method is to introduce the following phenomenological kinetic relation for the evolution of the transformation:

$$\dot{\nu}_t = \begin{cases} \dot{\nu}_{t\max} \tanh(\frac{1}{\vartheta} \cdot \frac{f_t - f_c}{f}), & \text{if } f_t > f_c \\ 0, & \text{otherwise} \end{cases} \tag{19}$$

where f_c stands for the critical value of the transformation driving force. The parameter $\dot{v}_{t\max}$ (maximum transformation rate) and ϑ (viscosity-like parameter) determine the rate dependence of the transformation kinetic law.

In this paper, a modified framework is proposed based on the prior arts mentioned above, which reflect the micro deformation mechanism of TWIP steel during the crystal deformation process. This modified model is developed within a multi-scale framework and uses the results from the crystallographic theory of martensitic transformation (Ball and James, 1987, Turteltaub and Suiker, 2005) and deformation twinning (Kalidindi, 1998). The martensitic transformation and twinning are coupled to a single-crystal plasticity model for FCC metals in order to account for plastic deformation in detail. The coupling among slip, twinning and martensitic transformation is derived using a thermodynamically consistent framework.

Fig.3 illustrates the decomposition of the global deformation gradient $\mathbf{F}$ when a twin system and martensitic transformation system work. The intermediate configuration is divided into four stages according to different mechanisms acting on the crystal: transformation, slip, twinning and twin rotation, successively. And the deformation quantities of transformation, slip and twinning are $\Delta\gamma^t$, $\Delta\gamma^\alpha$ and $\Delta\gamma^\beta$, respectively. The reference configuration is then transformed into the current configuration through the four stages.

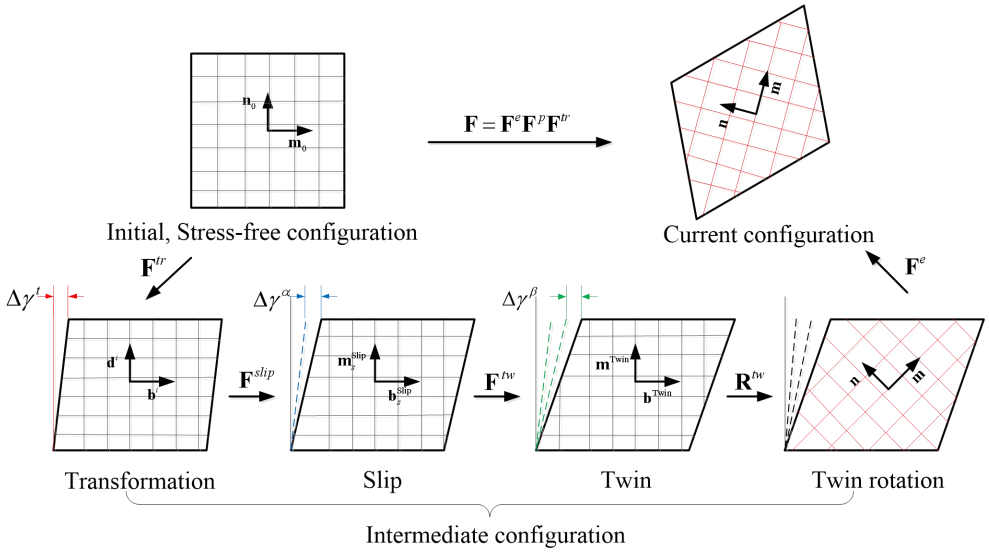

Fig.3. The improvement of classic intermediate configuration into five configurations is illustrated and the corresponding decomposition of deformation gradient **F** into the elastic, plastic and transformation parts is described.

Therefore, the evolution of the plastic deformation gradient $\mathbf{F}^p$, represented by the plastic velocity gradient $\mathbf{L}_\mathrm{p}$, is described by the following in the rate form:

$$\mathbf{L}_\mathrm{p} = \dot{\mathbf{F}}^p \cdot \mathbf{F}^{p^{-1}} = \sum_{\alpha=1}^{N_{slip}} \dot{\gamma}^\alpha \mathbf{S}_s^{Slip} + \sum_{\beta=1}^{N_{twin}} \dot{\gamma}^\beta \mathbf{S}_t^{Twin} \tag{20}$$

where N_{slip} is the number of slip systems, N_{twin} the number of twin systems and $\dot{\gamma}^\alpha$ (α = 1 to N_{slip}) the rate of slip shear from each possible slip system, $\dot{\gamma}^\beta$ (β = 1 to N_{twin}) the rate of twin shear. Meanwhile, $\mathbf{S}_s^{Slip} = \mathbf{n}^\alpha \otimes \mathbf{m}^\alpha$ is the Schmid tensor produced by a unit slip on system *s*, and $\mathbf{S}_t^{Twin}$ is the Schmid tensor produced by a unit twin on system *t*.

In carbon steels, the martensitic phase is relatively brittle with low dislocation activity, presumably due to the high level of interstitial carbon that prevents plastic slip. Consequently, it is assumed that plastic deformation only happens in the austenitic phase and not in the martensitic phase (Furnémont et al., 2002; Tjahjanto et al., 2008a, b). In addition, twinning cannot occur in twin region and martensite phase. Particularly, the martensite phase could only have elastic deformation due to this reason. Actually, the plastic deformation of thin-plate martensite phase cannot frequently occur due to its high carbon concentration. Furthermore, the model of transformation proposed by Turteltaub et al. (2005) is more focused on the thin-plate martensite phase. Consequently, there is less deviation in between the modeling and experiment.

Based on the framework mentioned above and considering the similarity in describing the velocity gradient of slip, twinning and transformation, the velocity gradient $\mathbf{L}_\mathrm{p}$ is extended based on the contributions from the characteristic twin shear and martensitic transformation

for FCC crystal structures and formulated in the following:

$$\mathbf{L}_{\mathrm{p}} = \dot{\mathbf{F}}^{p} \cdot \mathbf{F}^{p^{-1}} = v_{\mathrm{A}} \left(\sum_{\alpha=1}^{N_{slip}} \dot{\gamma}^{\alpha} \mathbf{S}_{s}^{Slip} + \sum_{\beta=1}^{N_{twin}} \dot{\gamma}^{\beta} \mathbf{S}_{t}^{Twin} \right) + \sum_{t=1}^{N_{trans}} \dot{v}_{t} \mathbf{S}_{t}^{Trans} \tag{21}$$

where N_{trans} is the number of transformation systems. The fundamental material parameters in Eq. (21) are the volume fraction v_{A} ($v_{\mathrm{A}} = 1 - v_{\mathrm{M}}$; $v_{\mathrm{M}} = \sum_{t=1}^{N_{trans}} v_{t}$) of austenite, the volume fraction v_{t} of each possible type (t = 1 to N_{trans}) of martensite plate, which are summed to the total martensite volume fraction v_{M} . $\mathbf{S}_{t}^{Trans} = \mathbf{b}_{t}^{Trans} \otimes \mathbf{m}_{t}^{Trans}$ is the Schmid tensor produced by the transformation of austenite to a type t martensite plate, where $\mathbf{b}_{t}^{Trans}$ is the average transformation direction and $\mathbf{m}_{t}^{Trans}$ is the habit plane normal.

In this paper, the modified deformation gradient is considered as a geometric quantity related to deformation which contains the crystallographic information of slip, twinning and transformation so that the phenomenological approach in describing the transformation could be associated with CP approach. And the change of the velocity gradient would influence the mesoscopic constitutive model in order to make a contribution to the macroscopic response. Therefore, it is necessary to make a further step in describing the constitutive model at mesoscopic scale. Although the phenomenological method in introducing the transformation model is well established, it really gives a quantitative analysis of the state variables such as transformation volume fraction and driving force, etc. at mesoscopic scale based on thermomechanics. In addition, the phenomenological description of transformation model is given in the framework of CP approach in order to make an intuitive understanding.

2.3 Establishment of constitutive relation

In this paper, the constitutive relation is established using rate-dependent approach. The rate-dependent theory arises from the regularization of the rate-independent theory. This is

useful from an algorithmic point of view as solving a problem with multiple yield surfaces is complex. In the rate-dependent formulation, the Kuhn-Tucker-type loading conditions used in the rate-insensitive approach are replaced by a constitutive evolution equation for plastic slips on slip systems (Asaro and Needleman, 1985). Actually, the evolution equations of plastic flow rule contain yield condition, loading/unloading criterion and consistency condition. Therefore, in the rate-sensitive model, there is no yield condition and no loading/unloading criterion applied. But it is necessary to articulate the yield condition for rate-dependent model of FCC crystals. In this research, the random one among the 12 slip systems will be activated as long as the resolved shear stress exceeds its critical value, i.e. onset of plastic deformation, according to the TWIP crystal structure. In the similar way, the twin growth and martensite nucleation will occur with the twinning volume fraction and transformation driving force achieving the critical value, respectively. To fully represent the constitutive relation, the plastic flow rule and hardening law are given in the following.

2.3.1 Flow rule

In the rate-dependent crystal plasticity, the shear rate of slip systems can be obtained directly by the decomposition of shear stress such that the uncertainty caused by the activation of slip systems can be avoided. The evolution equation for each micro shear rate can be typically specified as follows: (Pierce et al. 1982)

$$\dot{\gamma}^{\alpha}=\dot{\gamma}_0\left|\frac{\tau^{\alpha}}{s^{\alpha}}\right|^{1/m}\operatorname{sign}\left(\tau^{\alpha}\right) \tag{22}$$

where τ^{α} is the resolved shear stress on the slip system α. s^{α} is the slip resistance for the slip system α. m is the strain rate sensitivity factor. $\dot{\gamma}_0$ is a reference shear rate which is taken to be the same for all the slip systems and equals to 0.001 s^{-1} (Kalidindi, 2001; Li et

al., 2008), unless otherwise stated.

The same power law is adopted to describe the evolution of the deformation twin volume fraction (Kalidindi, 2004) as:

$$\dot{\gamma}^{\beta}=\dot{\gamma}_0\left(\frac{\tau^{\beta}}{s_{\mathrm{tw}}^{\beta}}\right)^{1/m},\ \text{if } \tau^{\beta}>0;\quad \dot{\gamma}^{\beta}=0,\ \text{if } \tau^{\beta}\le 0 \tag{23}$$

where τ^{β} and s_{tw}^{β} represent the resolved shear stress on a twin system and the twin resistance of that twin system, respectively. The constraints on Eq. (23) indicate that the twinning deformation is directional and the twin volume fraction is always positive. The sum of the twinned volumes cannot exceed the grain volume, and the twinned regions are not allowed to untwin.

The evolution of the martensite fraction during transformation follows the rate-dependent kinetic formulation, as Eq. (19) shows (Turteltaub and Suiker, 2005).

2.3.2 Hardening law

Description of the evolution of the slip and twin resistances in plastic deformation has been a very difficult problem in the development of robust crystal plasticity models for FCC metals such as TWIP steel. The slip-twin interaction is fairly complex, and there is thus far only a limited amount of quantitatively experimental data available. Some of the most successful phenomenological descriptions have been the saturation-type hardening laws that can be generically expressed as: (Salem et al., 2005)

$$\dot{s}^{\alpha}=h_s^{\alpha}\left(1-\frac{s^{\alpha}}{s_s^{\alpha}}\right)\sum_{\alpha=1}^{N_{slip}}\dot{\gamma}^{\alpha} \tag{24}$$

where h_s^{α} and s_s^{α} represent the hardening rate and the saturated value associated with the slip system α, respectively.

In this study, only considering the twinning resistance which is proportional to slip resistance, the evolution of twinning resistance could be shown as: (Salem et al., 2005)

$$s_{tw}^{\beta} = 1.2 s^{\alpha} \tag{25}$$

Recently, Salem et al. (2005) used the extended versions of the saturation-type hardening functions to capture the complex interactions between slip and twinning in the following:

$$h_s^{\alpha} = h_s \left(1 + C\left(\sum f^{\beta}\right)^b\right) \tag{26}$$

$$s_s^{\alpha} = s_{s0} + s_{pr}\left(\sum f^{\beta}\right)^{0.5} \tag{27}$$

In this paper, the additional mechanism such as hardening of slip resistance by martensitic transformation is not incorporated in the current framework although it indeed makes contribution to hardening effect. The plastic flow in martensite block could be assumed to take place by crystallographic slip on {110} <111> and {112} <111> slip systems for low-carbon martensite steel, dual-phase steel and TRIP-assisted steel (Ghassemi-Armaki, et al., 2013; Chen et al., 2014; Srivastava et al., 2015). However, for the TWIP steel with a relative higher carbon content (0.6C and 0.8C, wt%), there is less martensite although slip exists in **product martensite** (Koyama et al., 2011). In addition, it is noted that the martensite phase in TWIP steel with high carbon content, similar to high-carbon steels, is relatively brittle with low dislocation activity, probably due to the high level of interstitial carbon that prevents plastic slip (Tjahjanto et al., 2008a, b). Consequently, in this research, martensite is considered as a reinforced phase to cut the austenitic grains. **The hardening effect by martensite phase reflects in refining grains via considering martensite phase as barriers** The constitutive relations of TWIP steel based on the classic framework of elasto-plastic theory are given in **Box 1**.

Box 1. Constitutive model considering slip, twinning, transformation of TWIP steel.

1. Stress-strain relationship

$$\mathbf{T}^e = \Re : \mathbf{E}^e$$

$$\mathbf{E}^e = \frac{1}{2}\left(\mathbf{F}^{e^T} \cdot \mathbf{F}^e - \mathbf{I}\right)$$

$$\mathbf{T}^e = \mathbf{F}^{e^{-1}} \left\{\det\left(\mathbf{F}^e\right) \cdot \boldsymbol{\sigma}\right\} \mathbf{F}^{e^{-T}}$$

2. Flow rule

Slip rate : $\dot{\gamma}^\alpha = \dot{\gamma}_0 \left|\frac{\tau^\alpha}{s^\alpha}\right|^{1/m} \operatorname{sign}\left(\tau^\alpha\right)$

Shear rate of twining system: $\begin{cases} \dot{\gamma}^\beta = \dot{\gamma}_0 \left(\frac{\tau^\beta}{s^\beta_{tw}}\right)^{1/m}, \text{if } \tau^\beta > 0 \\ \dot{\gamma}^\beta = 0, \text{if } \tau^\beta \le 0 \end{cases}$

Evolution of martensite volume fraction: $\dot{v}_t = \begin{cases} \dot{v}_{t\max} \tanh\left(\frac{1}{\vartheta} \cdot \frac{f_t - f_c}{f_c}\right), & if\ f_t > f_c \\ 0, & \text{otherwise} \end{cases}$

3. Hardening law

$$\dot{s}^\alpha = h_s^\alpha \left(1 - \frac{s^\alpha}{s_s^\alpha}\right) \sum_{\alpha=1}^{N_{slip}} \dot{\gamma}^\alpha$$

$$s_{tw}^\beta = 1.2 s^\alpha$$

$$h_s^\alpha = h_s \left(1 + C\left(\sum f^\beta\right)^b\right)$$

$$s_s^\alpha = s_{s0} + s_{pr}\left(\sum f^\beta\right)^{0.5}$$

3. Numerical implementation

3.1 Update of state variables

Asaro and Needleman (1985) proposed the rate dependent numerical algorithm and promoted by Kalidindi et al. (1992), Marin and Dawson (1998). In the typical "implicit" finite element procedures that use nonlinear constitutive models, the discretized principle of virtual work, which enforces the equilibrium and boundary conditions in a weak sense, generates an estimated incremental displacement field which is used to calculate the values of integration

point of the second PK stress $\mathbf{T}$, the resistance to slip $\mathbf{s}$ and other field variables at the end of a time increment. In this paper, the full-implicit algorithm was adopted since it has an advantage in describing the multi-internal variables and multi-yield surfaces than that of explicit algorithm. It is noted that the reorientations of the twinned grains need to be determined by introducing the definition of the saturated value of twin volume fraction before the update of state variables. The saturated value of twin volume fraction can be attributed to the intense twin-twin and slip-twin interactions that increase the difficulty of producing new twins in the matrix at high strain level. Therefore, the reorientations of these grains may happen when the twin volume fraction reaches the saturated value. The threshold for the twin volume fraction based on the experiments by Renard et al., (2012) to judge if the twins rotate is introduced. Also, the contribution of the transformation is calculated whether the driving force satisfies the critical value. The update of state variables and the numerical implementation of the algorithms should be described in details since it is simplified in many researches such as Manchiraju and Anderson (2010).

To perform the incremental update of the state variables, firstly, a set of primary variables are identified: (a) Cauchy stress; (b) deformation gradient $\mathbf{F}$; (c) information of slip systems ($\mathbf{m}_0^{\alpha}$, $\mathbf{n}_0^{\alpha}$), twinning systems ($\mathbf{m}_0^{\beta}$, $\mathbf{n}_0^{\beta}$), transformation systems ($\mathbf{m}_0^{t}$, $\mathbf{n}_0^{t}$); (d) plastic deformation gradient $\mathbf{F}^p$; (e) initial slip resistance s_0^{α}, initial twinning resistance s_0^{β} and transformation driving force f_t.

Accordingly, it is assumed that: (i) the time-dependent slip systems ($\mathbf{m}_0^{\alpha}$, $\mathbf{n}_0^{\alpha}$), twinning systems ($\mathbf{m}_0^{\beta}$, $\mathbf{n}_0^{\beta}$) and transformation systems ($\mathbf{m}_0^{t}$, $\mathbf{n}_0^{t}$) are known; (ii) the list of state variables $\left\{\mathbf{F}(t), \mathbf{T}(t), \mathbf{F}^p(t), s^i(t), f_t\right\}$ in each grain at time *t* are given; and (iii) an estimate of deformation gradient $\mathbf{F}(\tau)$ at time is also given. With these given information, the computational problems are considered to be a stable, accurate and efficient computation of:

(a) the twin volume fraction $f^{\beta}(\tau)$ of various twinning systems at time τ ; (b) rotation matrix $\mathbf{R}^{tw}(\tau)$; (c) $\left\{\mathbf{F}(\tau), \mathbf{T}(\tau), \mathbf{F}^{p}(\tau), s^{i}(\tau), f_{t}\right\}$ at time τ ; (d) the computation of Jacobian matrix to be used in Newton-type iterative method for revising the estimated displacements such that the updated stresses better satisfy the principle of virtual work at the end of the increment.

To start with, a fully-implicit time-integration of the evolution equation (21) for $\mathbf{F}^{p}$ is used to obtain:

$$\mathbf{F}_{n+1}^{p\ -1} = \mathbf{F}_{n}^{p^{-1}} \cdot (\mathbf{I} - \mathbf{L}_{(n+1)}^{p} \Delta t) \tag{28}$$

where the initial value of $\mathbf{L}_{(n+1)}^{p}$ equals to zero since there is no deformation of crystals originally, and $\mathbf{L}_{(n+1)}^{p}$ evolves according to Eq. (21).

Substituting Eq. (28) into Eq.(1), the following is obtained:

$$\mathbf{F}_{n+1}^{e} = \mathbf{F}_{n+1} \cdot \mathbf{F}_{n+1}^{p\ -1} = \mathbf{F}_{n+1}^{e\ tr} \cdot (\mathbf{I} - \mathbf{L}_{(n+1)}^{p} \Delta t) \tag{29}$$

where $$\mathbf{F}_{n+1}^{e\ tr} = \mathbf{F}_{n+1} \cdot \mathbf{F}_{n}^{p^{-1}} \tag{30}$$

Therefore, the right Cauchy-Green tensor can be expressed as:

$$\begin{aligned} \mathbf{C}_{n+1}^{e} &= \mathbf{F}_{n+1}^{e\ T} \cdot \mathbf{F}_{n+1}^{e} = (\mathbf{I} - \mathbf{L}_{(n+1)}^{p} \Delta t) \cdot \mathbf{F}_{n+1}^{e\ tr\ T} \cdot (\mathbf{I} - \mathbf{L}_{(n+1)}^{p} \Delta t) \\ &= \mathbf{C}_{n+1}^{e\ tr} - (\mathbf{L}_{(n+1)}^{p\ T} \cdot \mathbf{C}_{n+1}^{e\ tr} + \mathbf{C}_{n+1}^{e\ tr} \cdot \mathbf{L}_{(n+1)}^{p}) \Delta t \end{aligned} \tag{31}$$

where $$\mathbf{C}_{n+1}^{e\ tr} = \mathbf{F}_{n+1}^{e\ trT} \cdot \mathbf{F}_{n+1}^{e\ tr} \tag{32}$$

Substituting Eq.(31) into Eq. (4), the elastic strain is determined:

$$\mathbf{E}_{n+1}^{e} = \mathbf{E}_{n+1}^{e\ tr} - sym(\mathbf{C}_{n+1}^{e\ tr} \cdot \mathbf{L}_{(n+1)}^{p}) \Delta t \tag{33}$$

where $sym(\mathbf{C}_{n+1}^{e\ tr} \cdot \mathbf{L}_{(n+1)}^{p})$ is the symmetric part of $\mathbf{C}_{n+1}^{e\ tr} \cdot \mathbf{L}_{(n+1)}^{p}$ and $\mathbf{E}_{n+1}^{e\ tr}$ is formulated as:

$$\mathbf{E}_{n+1}^{e\ tr} = \frac{1}{2}(\mathbf{C}_{n+1}^{e\ tr} - \mathbf{I}) \tag{34}$$

substituting Eq.(33) into Eq. (3):

$$\mathbf{T}_{n+1} = \mathbf{T}_{n+1}^{\ tr} - \Re : sym(\mathbf{C}_{n+1}^{e\ tr} \cdot \mathbf{L}_{(n+1)}^{p})\Delta t \tag{35}$$

where

$$\mathbf{T}_{n+1}^{\ tr} = \Re : \mathbf{E}_{n+1}^{e\ tr} \tag{36}$$

Finally, substituting Eq.(21) into Eq. (35), there is the following:

$$\begin{aligned}\mathbf{T}_{n+1} = & \mathbf{T}_{n+1}^{tr} - \nu_{\mathrm{A}} \left\{ \sum_{\alpha=1}^{12} \left[\dot{\gamma}^{\alpha} \left(\boldsymbol{\tau}_{n+1}^{\alpha}, \mathbf{s}_{n+1}^{\alpha} \right) \Re : sym\left(\mathbf{C}_{n+1}^{e\ tr} \cdot \mathbf{S}_{0}^{\alpha} \right) \right] \right\} \Delta t \\ & + \nu_{\mathrm{A}} \left\{ \sum_{\beta=1}^{12} \left[\dot{\gamma}^{\beta} \left(\boldsymbol{\tau}_{n+1}^{\beta} \right) \Re : sym\left(\mathbf{C}_{n+1}^{e\ tr} \cdot \mathbf{S}_{0}^{\beta} \right) \right] \right\} \Delta t + \sum_{t=1}^{24} \left[\dot{v}_{t} (\boldsymbol{\tau}_{n+1}^{Trans}) \Re : sym\left(\mathbf{C}_{n+1}^{e\ tr} \cdot \mathbf{S}_{t}^{trans} \right) \right] \Delta t \end{aligned} \tag{37}$$

where

$$\begin{aligned} \boldsymbol{\tau}_{n+1}^{\alpha} &= \left(\mathbf{C}_{n+1}^{e} \cdot \mathbf{T}_{n+1} \right) : \mathbf{S}_{0}^{\alpha} \\ \boldsymbol{\tau}_{n+1}^{\beta} &= \left(\mathbf{C}_{n+1}^{e} \cdot \mathbf{T}_{n+1} \right) : \mathbf{S}_{0}^{\beta} \\ \boldsymbol{\tau}_{n+1}^{Trans} &= \left(\mathbf{C}_{n+1}^{e} \cdot \mathbf{T}_{n+1} \right) : \mathbf{S}_{0}^{Trans} \end{aligned} \tag{38}$$

The use of an implicit method ensures stability, but it requires an iterative approach to solving $\mathbf{T}_{n+1}$ and $\mathbf{s}_{n+1}^{\alpha}$.These equations are solved using a *two-level* iterative procedure. In the first level of iteration, Eq. (37) is solved for $\mathbf{T}_{n+1}$, keeping $\mathbf{s}_{n+1}^{\alpha}$ fixed at its best available estimate. A Newton-Raphson scheme is deemed to be the most efficient method for the incrementally non-linear problem. Eq. (37) is re designated in the form of residual:

$$\begin{aligned}\mathbf{R}(\mathbf{T}_{n+1}) = & \mathbf{T}_{n+1} - \mathbf{T}_{n+1}^{tr} + \nu_{\mathrm{A}} \left\{ \sum_{\alpha=1}^{12} \left[\dot{\gamma}^{\alpha} \left(\boldsymbol{\tau}_{n+1}^{\alpha}, \mathbf{s}_{n+1}^{\alpha} \right) \Re : sym\left(\mathbf{C}_{n+1}^{e\ tr} \cdot \mathbf{S}_{0}^{\alpha} \right) \right] \right\} \Delta t \\ & + \nu_{\mathrm{A}} \left\{ \sum_{\beta=1}^{12} \left[\dot{\gamma}^{\beta} \left(\boldsymbol{\tau}_{n+1}^{\beta} \right) \Re : sym\left(\mathbf{C}_{n+1}^{e\ tr} \cdot \mathbf{S}_{0}^{\beta} \right) \right] \right\} \Delta t + \sum_{t=1}^{24} \left[\dot{v}_{t} (\boldsymbol{\tau}_{n+1}^{Trans}) \Re : sym\left(\mathbf{C}_{n+1}^{e\ tr} \cdot \mathbf{S}_{t}^{trans} \right) \right] \Delta t \end{aligned} \tag{39}$$

Assuming that after *i*th iteration, $\mathbf{T}_{n+1}$ turns into $\mathbf{T}_{n+1}^{(i)}$ and its residual is $\mathbf{R}_{T}^{(i)}$:

$$\mathbf{R}_{T}^{(i+1)} = \mathbf{R}_{T}^{(i)} + \Delta \mathbf{R}_{T}^{(i)} = 0 \tag{40}$$

$$\Delta\mathbf{R}_T^{(i)} = \Delta\mathbf{T}_{n+1}^{(i)} + \nu_{\mathrm{A}}\left\{\sum_{\alpha=1}^{12}\left[\Re : sym\left(\mathbf{C}_{n+1}^{e\ tr}\cdot\mathbf{S}_0^{\alpha}\right)\frac{\partial\dot{\gamma}^{\alpha}}{\partial\tau^{\alpha}}\bigg|_{\left(\boldsymbol{\tau}_{n+1}^{\alpha(i)},\mathbf{s}_{n+1}^{\alpha(k)}\right)}\Delta\tau_{n+1}^{\alpha\ (i)}\right]\right\}\Delta t$$

where
$$+\nu_{\mathrm{A}}\left\{\sum_{\beta=1}^{12}\left[\Re : sym\left(\mathbf{C}_{n+1}^{e\ tr}\cdot\mathbf{S}_0^{\beta}\right)\frac{\partial\dot{\gamma}^{\beta}}{\partial\tau^{\beta}}\bigg|_{\left(\boldsymbol{\tau}_{n+1}^{\beta(i)},\mathbf{s}_{n+1}^{\beta(k)}\right)}\Delta\tau_{n+1}^{\beta\ (i)}\right]\right\}\Delta t \tag{41}$$
$$+\sum_{t=1}^{24}\left[\Re : sym\left(\mathbf{C}_{n+1}^{e\ tr}\cdot\mathbf{S}_t^{trans}\right)\frac{\partial\dot{v}_t}{\partial\tau^{Trans}}\bigg|_{\left(\boldsymbol{\tau}_{n+1}^{Trans(i)}\right)}\Delta\tau_{n+1}^{Trans(i)}\right]\Delta t$$

According to Eqs. (34), (36) and (38), the following is obtained:

$$\begin{aligned}
\Delta\tau_{n+1}^{\alpha\ (i)} &= \left(\mathbf{C}_{n+1}^{e\ (i)}\cdot\mathbf{S}_0^{\alpha}\right):\Delta\mathbf{T}_{n+1}^{(i)} + \left(\mathbf{S}_0^{\alpha}\cdot\mathbf{T}_{n+1}^{(i)}\right):\Delta\mathbf{C}_{n+1}^{e\ (i)}\\
\Delta\tau_{n+1}^{\beta\ (i)} &= \left(\mathbf{C}_{n+1}^{e\ (i)}\cdot\mathbf{S}_0^{\beta}\right):\Delta\mathbf{T}_{n+1}^{(i)} + \left(\mathbf{S}_0^{\beta}\cdot\mathbf{T}_{n+1}^{(i)}\right):\Delta\mathbf{C}_{n+1}^{e\ (i)}\\
\Delta\tau_{n+1}^{Trans(i)} &= \left(\mathbf{C}_{n+1}^{e\ (i)}\cdot\mathbf{S}_0^{Trans}\right):\Delta\mathbf{T}_{n+1}^{(i)} + \left(\mathbf{S}_0^{Trans}\cdot\mathbf{T}_{n+1}^{(i)}\right):\Delta\mathbf{C}_{n+1}^{e\ (i)}
\end{aligned} \tag{42}$$

where
$$\Delta\mathbf{C}_{n+1}^{e\ (i)} = 2\Re^{-1} : \Delta\mathbf{T}_{n+1}^{(i)} \tag{43}$$

The incremental state variables of slip systems, twinning systems and transformation systems are expressed as, respectively:

$$\begin{aligned}
\Delta\tau_{n+1}^{\alpha\ (i)} &= \mathbf{A}_{\alpha}^{(i)} : \Delta\mathbf{T}_{n+1}^{(i)}\\
\Delta\tau_{n+1}^{\beta\ (i)} &= \mathbf{A}_{\beta}^{(i)} : \Delta\mathbf{T}_{n+1}^{(i)}\\
\Delta\tau_{n+1}^{Trans(i)} &= \mathbf{A}_{t}^{(i)} : \Delta\mathbf{T}_{n+1}^{(i)}
\end{aligned} \tag{44}$$

where
$$\begin{aligned}
\mathbf{A}_{\alpha}^{(i)} &= \mathbf{C}_{n+1}^{e\ (i)}\cdot\mathbf{S}_0^{\alpha} + 2\Re^{-1} : \left(\mathbf{S}_0^{\alpha}\cdot\mathbf{T}_{n+1}^{(i)}\right)\\
\mathbf{A}_{\beta}^{(i)} &= \mathbf{C}_{n+1}^{e\ (i)}\cdot\mathbf{S}_0^{\beta} + 2\Re^{-1} : \left(\mathbf{S}_0^{\beta}\cdot\mathbf{T}_{n+1}^{(i)}\right)\\
\mathbf{A}_{t}^{(i)} &= \mathbf{C}_{n+1}^{e\ (i)}\cdot\mathbf{S}_0^{Trans} + 2\Re^{-1} : \left(\mathbf{S}_0^{Trans}\cdot\mathbf{T}_{n+1}^{(i)}\right)
\end{aligned} \tag{45}$$

Finally, the *i*th corrected stress field is obtained as follows:

$$\Delta\mathbf{T}_{n+1}^{(i)} = \mathbf{B}^{(i)^{-1}} : \mathbf{R}_T^{(i)} \tag{46}$$

$$\mathbf{B}^{(i)} = \mathbf{I} + \nu_{\mathrm{A}}\left\{\sum_{\alpha=1}^{12}\left[\frac{\partial\dot{\gamma}^{\alpha}}{\partial\tau^{\alpha}}\bigg|_{\left(\boldsymbol{\tau}_{n+1}^{\alpha(i)},\mathbf{s}_{n+1}^{\alpha(k)}\right)}\left[\Re : sym\left(\mathbf{C}_{n+1}^{e\ tr}\cdot\mathbf{S}_0^{\alpha}\right)\right]\otimes\mathbf{A}_{\alpha}^{(i)}\right]\right\}\Delta t$$

where
$$+\nu_{\mathrm{A}}\left\{\sum_{\beta=1}^{12}\left[\frac{\partial\dot{\gamma}^{\beta}}{\partial\tau^{\beta}}\bigg|_{\left(\boldsymbol{\tau}_{n+1}^{\beta(i)}\right)}\left[\Re : sym\left(\mathbf{C}_{n+1}^{e\ tr}\cdot\mathbf{S}_0^{\beta}\right)\right]\otimes\mathbf{A}_{\beta}^{(i)}\right]\right\}\Delta t \tag{47}$$
$$+\sum_{t=1}^{24}\left[\frac{\partial\dot{v}_t}{\partial\tau^{Trans}}\bigg|_{\left(\boldsymbol{\tau}_{n+1}^{Trans(i)}\right)}\left[\Re : sym\left(\mathbf{C}_{n+1}^{e\ tr}\cdot\mathbf{S}_t^{trans}\right)\right]\otimes\mathbf{A}_{t}^{(i)}\right]\Delta t$$

I is the fourth order unit tensor. The convergence condition must be given as:

$$\left|\Delta T_{ij}\right| < \eta s_0 \tag{48}$$

where s_0 is the initial value of the slip system resistance and η is a numerical constant.

Based on the N-R iteration algorithm, the update of the second PK stress $\mathbf{T}_{n+1}^{(i+1)}$ is obtained in the following:

$$\mathbf{T}_{n+1}^{(i+1)} = \mathbf{T}_{n+1}^{(i)} + \Delta\mathbf{T}_{n+1}^{(i)} \tag{49}$$

In the second level of iterations, a fully implicit integration of the hardening law (24) for the evolution of the slip system resistances yields:

$$\mathbf{s}_{n+1}^{\alpha(i)} = \mathbf{s}_n^{\alpha(i)} + \mathbf{h}_s^{\alpha(i)}\left(1 - \frac{\mathbf{s}_n^{\alpha(i)}}{\mathbf{s}_s^{\alpha(i)}}\right)\sum_{\alpha=1}^{12}\dot{\gamma}^{\alpha}\Delta t \tag{50}$$

By fixing the value of $\mathbf{T}_{n+1}$, the update of slip resistance $\mathbf{s}_{n+1}^{\alpha}$ can be obtained using the similar method articulated in the following:

(a) Eq. (24) is rewritten in the form of residual:

$$\mathbf{R}\left(\mathbf{s}_{n+1}^{\alpha}\right) = \mathbf{s}_{n+1}^{\alpha} - \mathbf{s}_n^{\alpha} - \mathbf{h}_s^{\alpha}\left(1 - \frac{\mathbf{s}_n^{\alpha}}{\mathbf{s}_s^{\alpha}}\right)\sum_{\alpha=1}^{12}\dot{\gamma}^{\alpha}\Delta t \tag{51}$$

(b) Assuming after *i*th iteration, $\mathbf{s}_{n+1}^{\alpha}$ turns into $\mathbf{s}_{n+1}^{\alpha\ (i)}$ and its residual is $\mathbf{R}\left(\mathbf{s}_{n+1}^{\alpha\ (i)}\right)$:

$$\mathbf{R}\left(\mathbf{s}_{n+1}^{\alpha\ (i+1)}\right) = \mathbf{R}_s^{\alpha(i)} + \Delta\mathbf{R}_s^{\alpha(i)} = 0 \tag{52}$$

where

$$\Delta\mathbf{R}_s^{\alpha(i)} = \left|\mathbf{s}_{n+1}^{\alpha\ (i)} - \mathbf{s}_n^{\alpha(i)}\right| \tag{53}$$

The update of slip resistance $\mathbf{s}_{n+1}^{\alpha\ (i+1)}$ is then obtained until the convergence condition is satisfied.

A consistent tangent modulus or algorithmic tangent modulus should be provided to ensure the quadratic convergence rate (Chung et al., 2005) in the implicit finite element scheme. In the present work, numerical approximation of the tangent modulus is obtained by perturbing the deformation gradient at a given time step. Using the perturbed deformation gradient, the

perturbed Cauchy stress tensor $\boldsymbol{\sigma}(\mathbf{F}^{per,(ij)})$ is computed following the typical time integration scheme and finally the algorithmic tangent modulus is approximated as (Sun et al. 2008, Lee et al., 2010)

$$\mathbf{A}^{consist,(ij)} \cong \frac{\boldsymbol{\sigma}(\mathbf{F}^{per,(ij)}) - \boldsymbol{\sigma}}{\varepsilon} \tag{54}$$

where ε is a perturbation parameter and is set to 10^{-5} in this research. In Eq. (54), $\mathbf{F}^{per,(ij)}$ denotes the perturbed deformation gradient at the time step $t + \Delta t$ and the index (i, j) reflects the symmetry of tensor.

3.2 Numerical implementation algorithms into the implicit FEM

The complete time-integration procedure of the time dependent crystal plasticity model for the present model is listed in Box 2. And, the detailed Newton-Rhapson procedure in the algorithm can be further referred to the previous literature, especially by Kalidindi and co-authors (1992, 1998). As shown in Box 2, plastic deformation gradient $\mathbf{F}^{p}_{n+1}$ and the second PK stress $\mathbf{T}_{n+1}$ are calculated in order to determine the Cauchy stress $\boldsymbol{\sigma}_{n+1}$ and the elastic right Cauchy-Green tensor $\mathbf{C}^{e}_{n+1}$ .Then the detailed task of determining the residual of the second PK stress $\mathbf{T}_{n+1}$ and slip resistance $\mathbf{s}^{\alpha}_{n+1}$ are done with respect to the Newton-Raphson method, which would be useful to obtain the increment of internal variables and further update the state variables (slip increment, twinning increment, etc.). Particularly, Fig.4 shows the specific flow diagram of the numerical algorithm into implicit finite element method in terms of the order listed in Box 2.

Box 2. Summary of the stress update algorithm for the rate-dependent constitutive model.

Step 1 : Compute plastic deformation gradient $\mathbf{F}_{n+1}^{p}$ and the second PK stress $\mathbf{T}_{n+1}$

$\mathbf{L}_0^p = 0$

$\mathbf{F}_{n+1}^{p\ -1} = \mathbf{F}_n^{p\ -1} \cdot (\mathbf{I} - \mathbf{L}_{(n+1)}^p \Delta t)$ ($\mathbf{L}_{(n+1)}^p$ evolves according to Eq. (21))

$\mathbf{F}_{n+1}^{e\ tr} = \mathbf{F}_{n+1} \cdot \mathbf{F}_n^{p\ -1}$

$\mathbf{F}_{n+1}^{e} = \mathbf{F}_{n+1} \cdot \mathbf{F}_{n+1}^{p\ -1} = \mathbf{F}_{n+1}^{e\ tr} \cdot (\mathbf{I} - \mathbf{L}_{(n+1)}^p \Delta t)$

$\mathbf{C}_{n+1}^{e\ tr} = \mathbf{F}_{n+1}^{e\ trT} \cdot \mathbf{F}_{n+1}^{e\ tr}$

$\mathbf{C}_{n+1}^{e} = \mathbf{F}_{n+1}^{e\ T} \cdot \mathbf{F}_{n+1}^{e} = \mathbf{C}_{n+1}^{e\ tr} - (\mathbf{L}_{(n+1)}^{p\ T} \cdot \mathbf{C}_{n+1}^{e\ tr} + \mathbf{C}_{n+1}^{e\ tr} \cdot \mathbf{L}_{(n+1)}^{p}) \Delta t$

$\mathbf{T}_{n+1}^{tr} = \mathfrak{R} : \mathbf{E}_{n+1}^{e\ tr} = \mathfrak{R} : \frac{1}{2}(\mathbf{C}_{n+1}^{e\ tr} - \mathbf{I})$

$\mathbf{T}_{n+1} = \mathbf{T}_{n+1}^{tr} - \mathfrak{R} : sym(\mathbf{C}_{n+1}^{e\ tr} \cdot \mathbf{L}_{(n+1)}^{p}) \Delta t$

$\mathbf{T}_{n+1} = \mathbf{F}_{n+1}^{e\ -1} \cdot \left\{ \det(\mathbf{F}_{n+1}^{e}) \cdot \boldsymbol{\sigma}_{n+1} \right\} \cdot \mathbf{F}_{n+1}^{e\ -T}$,

Step 2 : Setting initial values

$i = 0 : \mathbf{T}_{n+1}^{(0)} = \mathbf{T}_n$, $\mathbf{s}_{n+1}^{\alpha(0)} = \mathbf{s}_n$, $\Delta\boldsymbol{\tau}^{(0)}$=0, and $\boldsymbol{\tau}_{n+1}^{\alpha(0)}$, $\boldsymbol{\tau}_{n+1}^{\beta(0)}$, $\boldsymbol{\tau}_{n+1}^{Trans(0)}$ are initialized using Eq. (38)

Step 3 : Compute updated value of second PK stress $\mathbf{T}_{n+1}^{(k+1)}$ with fixed slip resistance

Calculate $\Delta\mathbf{R}_T^{(i)}$ and $\mathbf{B}^{(i)}$ using Eqs. (41,47)

$\Delta\tau_{n+1}^{\alpha\ (i)} = \mathbf{A}_{\alpha}^{(i)} : \Delta\mathbf{T}_{n+1}^{(i)}$; $\Delta\tau_{n+1}^{\beta\ (i)} = \mathbf{A}_{\beta}^{(i)} : \Delta\mathbf{T}_{n+1}^{(i)}$; $\Delta\tau_{n+1}^{Trans(i)} = \mathbf{A}_{t}^{(i)} : \Delta\mathbf{T}_{n+1}^{(i)}$

Calculate $\mathbf{A}_{\alpha}^{(i)}$,$\mathbf{A}_{\beta}^{(i)}$ and $\mathbf{A}_{t}^{(i)}$ using Eq. (45)

$\mathbf{R}_T^{(i+1)} = \mathbf{R}_T^{(i)} + \Delta\mathbf{R}_T^{(i)} = 0$

$\Delta\mathbf{T}_{n+1}^{(i)} = \mathbf{B}^{(i)\ -1} : \mathbf{R}_T^{(i)}$

$\mathbf{T}_{n+1}^{(i+1)} = \mathbf{T}_{n+1}^{(i)} + \Delta\mathbf{T}_{n+1}^{(i)}$

If $\mathbf{R}\ (\mathbf{T}_{n+1}^{(i)}) < \mathrm{TOL}_1$, Then go to **step 4**,

Else, set $i \leftarrow i+1$,

go to **step 3**, until satisfying the convergence condition,

Step 4 : Compute the updated value of slip resistance $\mathbf{s}_{n+1}^{\alpha(i+1)}$

$\mathbf{s}_{n+1}^{\alpha(i+1)} = \mathbf{s}_{n+1}^{\alpha(i)} + \Delta\mathbf{s}_{n+1}^{\alpha(i)} = \mathbf{s}_{n+1}^{\alpha(i)} + \mathbf{h}_s^{\alpha(i)} \left(1 - \frac{\mathbf{s}_n^{\alpha(i)}}{\mathbf{s}_s^{\alpha(i)}} \right) \sum_{\alpha=1}^{12} \dot{\gamma}^{\alpha} \Delta t \quad \alpha \in (1,2,\ldots,12)$

$\mathbf{R}\ (\mathbf{s}_{n+1}^{\alpha(i)}) = \mathbf{s}_{n+1}^{\alpha(i)} - \mathbf{s}_n^{\alpha(i)} - \mathbf{h}_s^{\alpha(i)} \left(1 - \frac{\mathbf{s}_n^{\alpha(i)}}{\mathbf{s}_s^{\alpha(i)}} \right) \sum_{\alpha=1}^{12} \dot{\gamma}^{\alpha} \Delta t \quad \alpha \in (1,2,\ldots,12)$

If $\mathbf{R}\ (\mathbf{s}_{n+1}^{\alpha(i)}) < \mathrm{TOL}_2$, Then go to **step 5**,

Else, set $i \leftarrow i+1$,

go to **step 3**, until satisfying the convergence condition,

Step 5 : Update state variables

Slip increment $\Delta\gamma_{n+1}^{\alpha}$,Twinning increment $\Delta\gamma_{n+1}^{\beta}$,

inverse matirx of plastic deformation gradient $F_{n+1}^{p\ -1}$, Cauchy stress $\boldsymbol{\sigma}_{n+1}^{(i+1)}$

Step 6 : Compute consistent tangent modulus

$\mathbf{A}^{consist,(ij)} \cong \frac{\boldsymbol{\sigma}(\mathbf{F}^{per,(ij)}) - \boldsymbol{\sigma}}{\varepsilon}$

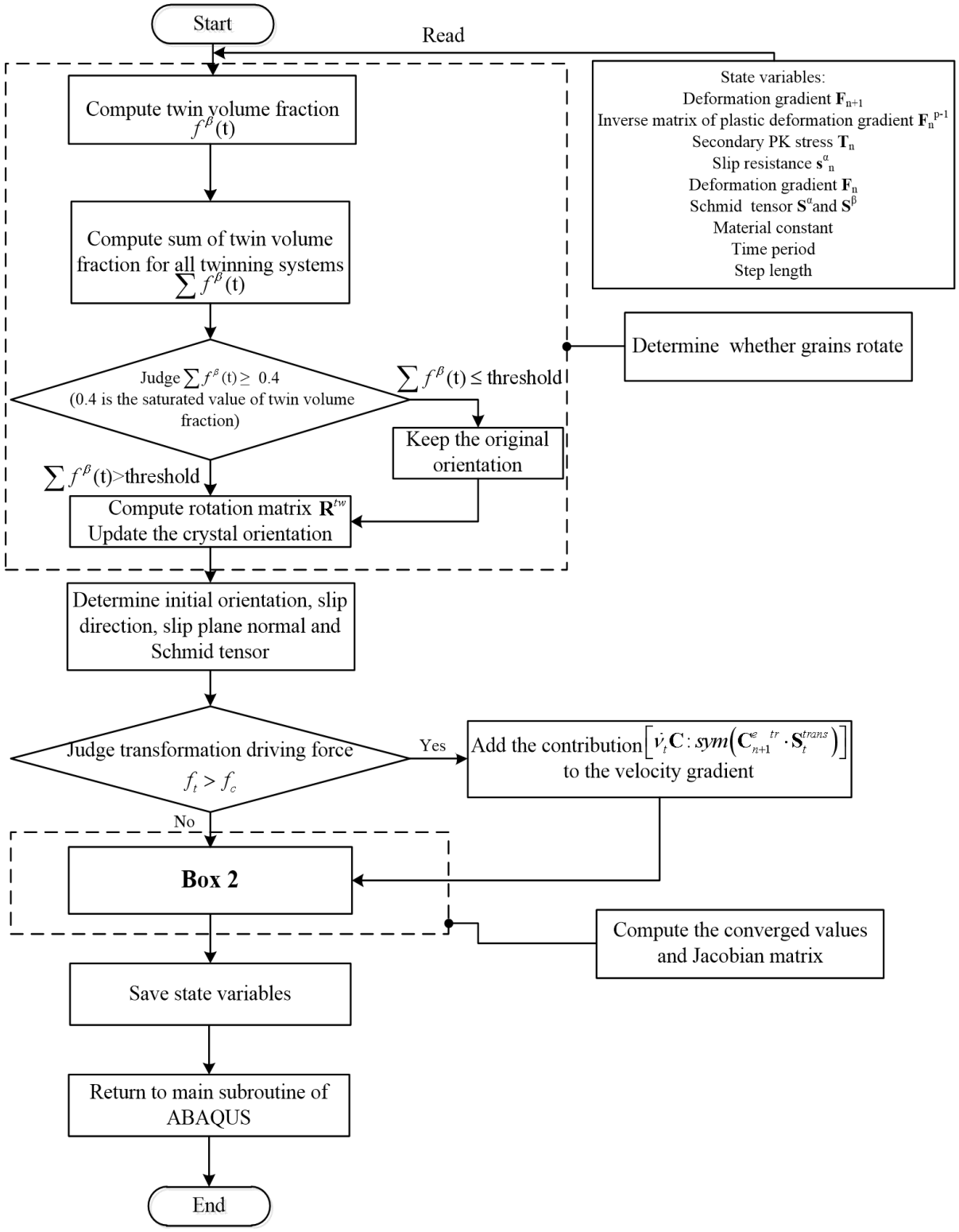

Fig.4. The flow chart of numerical algorithm into implicit FEM.

4. Simulation and discussion

4.1 Verification of the model

In terms of experimental investigation, Koyama et al. (2011) performed a tensile test on carbon-containing twinning induced plasticity (TWIP) steels at different temperatures (173, 223, 273, 294, and 373 K). The ε-martensitic transformation, deformation twinning, and dynamic strain aging were observed during tensile test. And also the characteristic deformation mode that contributes to work hardening rate changed with deformation temperature. For this work, the macroscopic responses with the experiment results of Fe–17Mn–0.6C TWIP steel are carefully corroborated.

Actually, initial texture plays an important role in microstructure evolution and hardening effect in tensile deformation. According to Koyama et al. (2011), from the treatment of Fe-17Mn-0.6C TWIP steel, the steel may have various kinds of textures such as recrystallization texture and transformation texture, etc.; the textures after hot rolling, however, are really not very obvious comparing with cold rolling. So the initial orientations of crystals are assumed to be stochastic in order to simplify the model, namely, the initial textures are neglected as an assumption in this research. Consequently, it is assumed that the orientations of all the crystals are given randomly before deformation. And in the simulation, the FEM global coordinate system is defined along the crystallographic axes.

Table 2 summarizes the final values adopted for the material parameters of crystallographic slip, twinning and transformation together with elastic tensors. With repeated trials via comparing the simulations with experimental results, the final choices of parametric combinations were obtained. The methods for determining the elastic tensors (C_{11}, C_{12}, C_{44}) of TWIP steel can be found according to the references by Pierce et al. (2013) and Gebhardt et al. (2011). The saturated value of twin volume fraction is identified by recording the twin volume fraction during the plastic deformation process (Renard et al., 2012), and the twins realize reorientation when the saturated value of twin volume fraction reaches the threshold. In this experiment, the evolution of twin volume fraction is shown to evolve following an

S-shape, i.e., the saturated value of twin volume fraction is set to be~0.4. Therefore, the saturated value of twin volume fraction is 0.4 to reflect the reorientation mechanism. The transformation parameters ($\dot{v}_{t\max}$, ϑ , f_c , θ_T , λ_T) are determined based on the material parameters study by prior arts (Manchiraju and Anderson, 2010; Turteltaub and Suiker, 2005). The material parameters used in the phase transformation model are presented based on the macroscopic properties of Fe-17Mn-0.6C TWIP steel (Koyama et al., 2011). Note that these experiments by Koyama et al. (2011) are reported to deform by martensitic transformation with negligible plastic deformation. Plasticity parameters (h_s , S_{s0} , S_{pr} , b, C, S_0^{α} , S_0^{β}) are calibrated from the stress-strain response. In the absence of enough experimental data to determine the plasticity parameters, a low strain rate sensitivity m = 0.02 and a reference strain rate $\dot{\gamma}_0$ =0.001 s^{-1} are assumed (Kalidindi et al., 1992). The large hardening in the experimental response dictates a large initial hardening rate (h_s = 800 MPa) and a large saturation hardness (S_{s0} =300MPa). The sensibility of plastic parameters has been analyzed in details in the previous work by Sun et al. (2015). A general determination of the value range and a sequencing analysis of these plastic parameters are given briefly here. Firstly, it is necessary to provide a sequence for determination of plastic parameters. The slip resistance S_0^{α} is obtained from the yield limit. The twinning hardening parameter b is then determined by the hardening rate curve. In addition, the parameter S_{pr} representing the effect of Hall-Petch mechanism is also obtained according to the strain hardening rate curve. Based on the aforementioned process, an approximate value range of the plastic parameters is listed:

1) The initial slip resistance S_0^{α} is linearly associated with the yield limit, and the value of the initial slip resistance range is 80~160 MPa.

2) A weakening tendency of the twinning hardening stage would appear with the

increasing twinning hardening parameter *b*, which ranges from 0 to 3.

3) The twinning resistance S_0^{β} is proportional to the slip resistance S_0^{α}, the ratio between the two variables is 1 to 1.3.

These predictions are compared with the polycrystalline experiment of Fe-17Mn-0.6C TWIP steel using the parameters for single crystals. In the present work, 3D polycrystalline aggregates are simulated using 1920 elements and each grain is meshed using a single 3D finite element (C3D8). In addition, each element has a different orientation to mimic a polycrystalline response. Unlike the modeling of single crystal, the polycrystalline situation is complicated by the fact that individual grain misorientations and deviations from ideal (single crystal) texture become important. This directly reflects from the number of grain orientations modeled in the numerical simulation and their efficiency in representing the real texture. The limited number of grains and their orientations are expected to affect the result. The primary goal here is to show that the developed constitutive model captures the trend adequately. The quantitative deviations may be ascribed to the limited information on the grain orientations and deviations from the real textures. Actually, to study the stress-strain behavior at grain level of polycrystalline materials, the particular attention is put on the selection of the minimum number of grains in the microstructure that can be considered as the representative volume element (RVE) of a sample subjected to plastic deformation (Szyndler and Madej, 2015, Zeng et al.,2015). In their researches, the strength of aggregates with more grain cells differs from the one with fewer cells and generally the stress-strain response using more grain cells may be closer to the experimental results. Therefore, in this research, the limited grain number may be a key factor that the predicted result deviates from the experimental data. Different initial textures show a great effect on the formability of AZ31 alloy sheets in deep drawing process (Zhang et al., 2014). This significant influence leads to the change of hardening effect, which could be referred to the explanation of the

deviation between the experimental data and simulated results during the plastic deformation process for the polycrystalline material. Since the initial texture is neglected, the deviation is assumed to be arising from this issue. Additional mechanisms such as hardening of slip by martensitic transformation and evolution of twin nucleation are not incorporated in the current framework.

Fig. 5 (a) compares the simulated macroscopic stress–strain responses for the polycrystal model with the experimental data. Even with the limited number of initial grain orientations, the general trends are well reproduced for all the curves. For the working temperature at 173K, a good agreement between the simulation and experiment could be observed before the strain reaches 0.2 and the deviation is less than 5%. However, a deviation increases gradually after the engineering strain of 0.2. In addition, for the temperature at 223K and 273K, a small deviation (~5%) from the experiments could be seen when the engineering strain is 0.35 and 0.4 respectively. In order to analyze the deviation of the stress-strain responses from experiment, the mechanisms should be considered during the tensile test. According to the deformation characteristics of Fe-17Mn-0.6C TWIP steel (Koyama et al., 2011), the ε-transformation could be observed at the temperature of 173, 223 and 273K. For the case of temperature above 273K, however, ε-transformation did not appear. So the macroscopic responses at the loading temperature of 173, 223 and 273K, including ε-transformation, were selected as the experimental evidence to verify the model. In this research, the hardening effect of plastic slip by transformation at microscopic level has not been considered but the crystallographic information of transformation at macroscopic level was introduced. It is reason for the deviation at the later period of deformation. Furthermore, the modeling of initial texture was simplified, but indeed it contributes to the hardening effect and microscopic evolution in tensile test. In fact, the serrated stress-strain curves are typically observed in TWIP steels due to the dynamic strain aging (Koyama et al. 2011). The

predicted curves do not capture the characteristics for the absence of dynamic strain aging modeling and the averaging approach in analyzing the simulation data. Finally, the coarse meshes (one element per grain) and the calibrated parameters should be mentioned as the probable factors which could result in the different deviations for all the curves.

In order to take a further step into the capability and validity of the proposed model, the comparison of strain-hardening curves is used as a measurement indicator. In Fig. 5 (b), it is also seen that the trends of the predicted hardening rate curves for polycrystalline TWIP steel agree reasonably with the experiments. An obvious increase of the strain hardening rate curve could be observed at the true strain of 0.15 and 0.35 at the temperature of 173, 273K, respectively. This issue would be explained by the introduction of transformation. However, for the hardening rate of all these temperatures, the deviation is also found due to the absence of strengthening of slip resistance by transformation.

With the material constants specified in the text, the following simulations are all based on the material constants shown in Table 2. To validate and verify the models and algorithms for modeling crystal deformation mechanisms, the mechanical behaviors of single crystal are simulated.

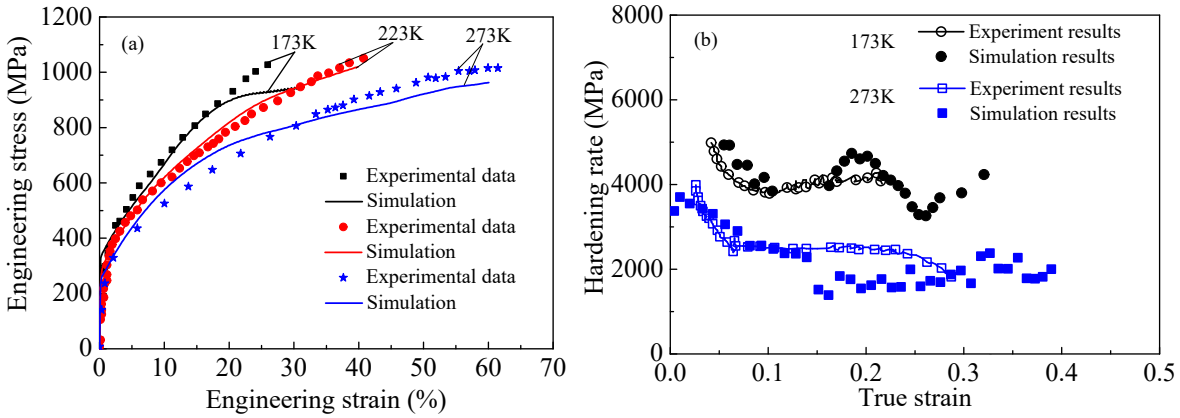

Fig.5. Comparison of (a) stress-strain responses and (b) work hardening rate from simulation with the experiments performed at different temperatures (Koyama et al., 2011).

Table 2. Material parameters in the constitutive relations calibrated for TWIP steel.

Initial hardening rate of slip system h_s (MPa)	800
Saturated value of slip resistance without twinning S_{s0} (MPa)	300
Hardening index of twinning *b*	3
Hardening coefficient of twinning *C*	10
Effect of Hall-Petch mechanism S_{pr} (MPa)	400
Initial slip resistance S_0^{α} (MPa)	90
Initial twinning resistance S_0^{β} (MPa)	108
Elastic constant C_{11}(GPa)	169
Elastic constant C_{12}(GPa)	125
Elastic constant C_{44}(GPa)	120
Rate sensitivity coefficient *m*	0.024
Reference shear rate $\dot{\gamma}_0$ (s^{-1})	0.001
Maximum transformation rate $\dot{v}_{t\max}$ (s^{-1})	0.003
Viscosity-like parameter ϑ	0.17
Critical energy barrier per unit volume for transformation f_c (MPa)	26
Equilibrium transformation temperature θ_T (K)	246
Latent heat of transformation per unit volume λ_T (MPa)	546

4.2 Effect of twinning and transformation on hardening

To investigate the effect of twinning on hardening for polycrystals from the perspective of deformation mechanism, a series of constitutive models to describe twin nucleation, propagation, growth and de-twinning for polycrystals have beendeveloped recently (Wang et al., 2013; Wu et al., 2015). Particularly, the deformation twinning and its hardening effect of magnesium single crystal was studied by usingnano-indentation (Shin et al., 2013; Zambaldi et al., 2015). For TWIP steel single crystal, it is necessary to articulate the twinning and transformation effect on the hardening of macroscopic response. The presented model is based on the slip-twinning model, so that it could reflect the mechanism of twinning on the

hardening of TWIP steel single crystal naturally. In addition, transformation on the hardening effect would be represented according to the developed model. Therefore, it is necessary to explain the interaction between the twinning and transformation and their contributions to the hardening of TWIP steel single crystals. In this research, Euler angles (10º, 0º, 35º) and (60º, 10º, 0º) are selected randomly in order to further study the hardening effect by using the proposed model. It is noted that in the finite element model, a cube is regarded as a single crystal and its side length is 10 mm. To achieve the engineering strain of 0.6 approximately, the cube was stretched with 6 mm along Y axis. The loading time is 600 s (i.e. strain rate is $0.001s^{-1}$) to satisfy a quasi-static condition. The stress-strain response after deformation and the hardening rate of Euler angle (10º, 0º, 35º) are shown in Fig. 6.

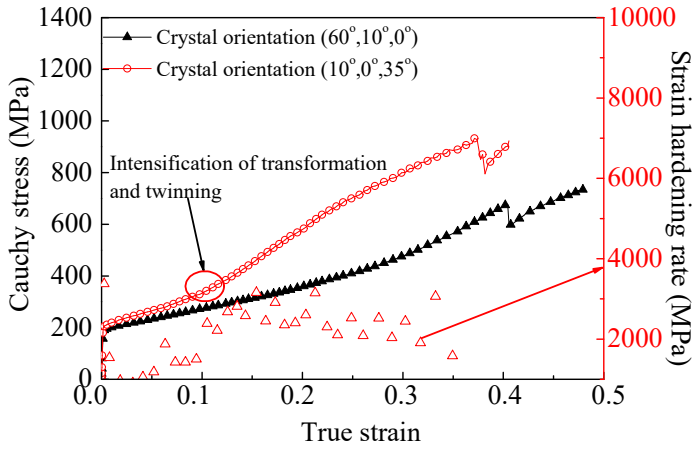

Fig.6. The effects of different Euler angles (10º, 0º, 35º) and (60º, 10º, 0º) on hardening for TWIP single crystal at the strain rate $0.001s^{-1}$ when the true strain reaches 0.4 and 0.48 respectively. And the strain hardening rate of Euler angle (10º, 0º, 35º) is given particularly.

It is obviously indicated in Fig.6 that both twinning and transformation have an effect on the hardening regardless of crystal orientations. Furthermore, the hardenability of Euler angle (10º, 0º, 35º) is apparently higher than that of Euler angle (60º, 10º, 0º). Particularly, an obvious increase of the stress-strain response for Euler angle (10º, 0º, 35º) could be observed

at the true strain of ~0.1, compared with that at the true strain of ~0.3 for Euler angle (60º, 10º, 0º). Meanwhile, this intensification of Cauchy stress can also be seen in the strain hardening rate curve of Euler angle (10º, 0º, 35º). In addition, the deviation between Euler angle (10º, 0º, 35º) and Euler angle (60º, 10º, 0º) increases after the true strain of ~0.1. Since twinning and transformation would have a significant influence on hardening of these two Euler angles, it is thus necessary to study the evolution of twin volume fraction and martensite phase transformation volume fraction to clarify their contributions to hardening. Therefore, the twin and transformation volume fraction of TWIP steel single crystals are simulated only for the Euler angle (10º, 0º, 35º).

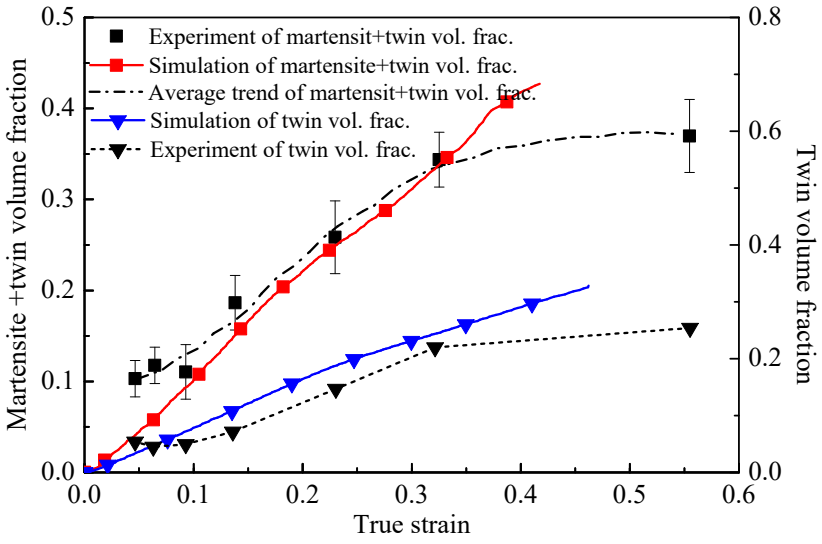

Fig.7. Sum of martensite and twin volume fractions versus strain for the TWIP steel single crystal with the Euler angle (10º, 0º, 35º), including its evolution of twin volume fraction against experimental results. (Pls pay attention: The text in the above figure overlaps with the curve, pls revise it)

To study the stress rising in the macroscopic response of TWIP steel single crystal with the Euler angle (10º, 0º, 35º), it is necessary to validate the reliability of the evolution of twin

volume fraction and transformation volume fraction during the uniaxial tensile test of the TWIP steel including twinning and ε-martensite transformation mechanisms. The experimental results obtained by prior researches (Ghasri-Khouzani and McDermid, 2015) are provided to address this issue. In prior arts, both mechanical twins and ε-martensite were observed during the deformation of Fe–22Mn–0.4C alloy. It is noted that in Fig. 7, the predictions of the evolution of twin volume fraction and martensite + twin volume fraction are similar to the ones of Fe–22Mn–0.4C steel in the experiments quantitatively and qualitatively. There are deviation between simulation and experiment, which could be attributed to some facts such as a slight difference of chemical composition, and experiment and simulation error. It is noted that in the presented model, the evolution of twin volume fraction and martensite + twin volume fraction are rising from zero, comparing with the non-zero value in experiments. The initial values are neglected for simplification since they are really small before plastic deformation. In addition, the trend of martensite + twin volume fraction appears to be saturated after the strain of ~0.4, but the prediction deviates from the experimental results. This issue could be caused by the dominating phase transformation on the secondary hardening in macroscopic response after the strain of ~0.4. Moreover, the increasing strain hardening rate of TWIP steel single crystal with the Euler angle (10º, 0º, 35º) could be ascribed to the strengthening of hardening caused by martensite phase transformation.

4.3 Stress drop for TWIP single crystals

For the single crystals dominated by the twinning-induced plasticity (TWIP) effect, the stress drop in the stress-strain response is considered as an interesting and existing mechanism caused by the twinning reorientation. However, it has not yet been fully explored. In the previous study, it is noted that in some single crystal materials with TWIP effect such as

copper single crystal with a certain orientation [541], the stress drop in the macroscopic response could be observed during the uniaxial tensile process and this could be attributed to the twinning reorientation (Niewczas et al., 2001). In addition, in the uniaxial tensile test of magnesium single crystal with the orientation of [0001], the initiation of $\{10\bar{1}2\}$ twins results in a sudden load drop and is accompanied by a 2−5% strain burst (Yu et al., 2012). It is reasonable to conclude that for the single crystals with TWIP effect under particular orientations during uniaxial tension, the reorientation of crystal due to twinning changes the ability of dislocations to move, which can lead to softening (Yu et al., 2012). However, for the compression tests of [0001] magnesium single crystal, it is noted that there is no obvious stress drop in the macroscopic response due to the nucleation of a **single** $\{10\bar{1}1\}$ **contraction twin resulting strain softening** instead of a sharp drop (Yu et al., 2012). Indeed, in the compression test of TWIP steel micro pillars with the diameter of 705nm and 3.9um with the approximate orientations of [001] and [136] respectively, it shows no distinct load drop in the experiments (Wu et al., 2012). It could be concluded that the stress drop, a non-typical phenomenon during uniaxial loading, is associated with crystal orientation andloading condition. Therefore, a detailed explanation is focused on these factors in this research to articulate how the stress drop is reproduced in mesoscale simulation.

4.3.1 Effect of crystal orientation and loading condition on stress drop

On the basis of the aforementioned experimental results for single crystals with TWIP effect, the crystal orientation associated with loading condition play a significant role in the evolution of macroscopic response, particularly in the stress drop. In addition, the crystal orientation may lead to a **prominent distinction** in uniaxial tensile test. Fig. 8 illustrates the evolution of macroscopic response for copper single crystals with certain orientations of [001] and [541]. It is found that for the copper single crystal with the orientation of [541], the mesoscale simulation reveals an obvious stress drop at the strain of ~0.65, compared with

the experimental results obtained by Niewczas et al. (2001). Since there is no phase transformation for the copper single crystal at the temperature of 4.2K (Niewczas et al., 2001), the simulation was carried out by using the crystal plasticity model considering slip and twinning. The stress drop was observed which could be attributed to the evolution of twin volume fraction. In order to articulate how the stress drop occurs, the twin volume fraction (dashed line) of the copper single crystal with the orientation of [541] is provided. Obviously, the twin volume fraction comes to saturated value when the stress drop reproduces. The reorientation of the crystal due to the saturated twin volume fraction leads to the activation of several other slip systems. It is revealed that the activation stress of slip system is considered to be smaller than that of twinning system. Consequently, a significant stress drop in the macroscopic response would be reproduced mainly caused by the evolution of twin volume fraction. Compared with the orientation of [541], a distinct macroscopic response and twin volume fraction of copper single crystal with the orientation of [001] was observed during the uniaxial tensile test. For this orientation, there is no stress drop in the stress strain response since the twin volume fraction is almost zero in the tensile test process. Therefore, the crystal orientation of single crystal with TWIP effect has a great influence on the macroscopic response due to the evolution of twin volume fraction.

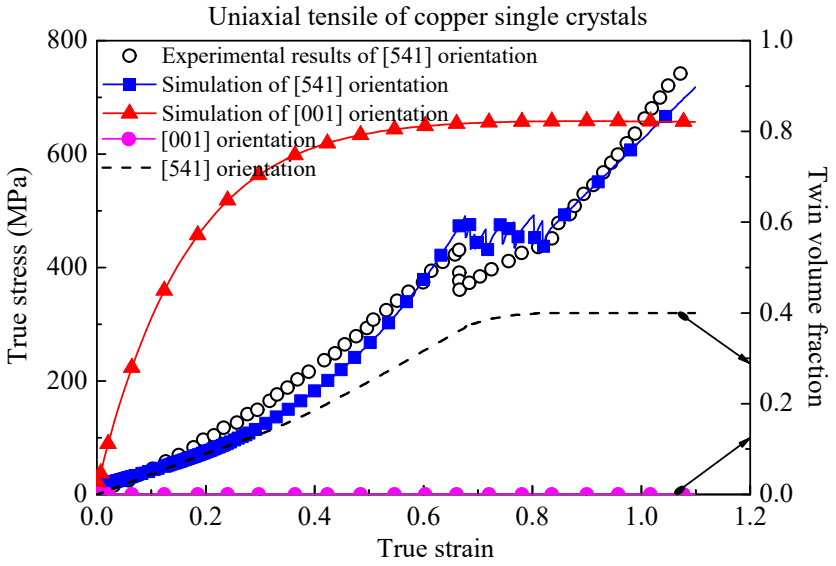

Fig.8. Evolution of macroscopic response for copper single crystals with the orientations of [001] and [541] and the twin volume fraction in uniaxial tensile test.

For the TWIP steel, the influence of loading condition on the evolution of macroscopic response could not be ignored, particularly for single crystal with TWIP effect (Yu et al., 2012, Wu et al., 2012). For the magnesium single crystal oriented at [0001], after twinning initiation, there is a significant difference between the compression and tensile tests in terms of both the twin structure and the corresponding mechanical data (Yu et al., 2012). In addition, - the TWIP steel micro pillar oriented at [136] in compression test did not show any load drop based on its load-displacement curve. Although there is no experimental evidence of TWIP steel single crystal oriented at [136]-under uniaxial tensile test to date, it could be possible the stress and strain response under uniaxial tensile could be different from that under compression**?????**. In Fig. 9, for the TWIP steel single crystal oriented at [136]-under uniaxial tensile and compression deformation, an apparent load drop in the load-displacement curve of uniaxial tensile occurs compared with that of uniaxial compression. Similarly, the evolution of twin volume fraction for these two loading conditions is given to articulate how the load drop occurs. Based on the analysis of crystal orientation effect, the load drop could be attributed to the saturated twin volume fraction. Consequently, the stress drop in macroscopic response of TWIP single crystals may be reproduced under a certain crystal orientation and loading condition. Therefore, this unique phenomenon cannot be ignored and needs in-depth exploration in terms of the mechanisms of deformation twinning for TWIP single crystals.

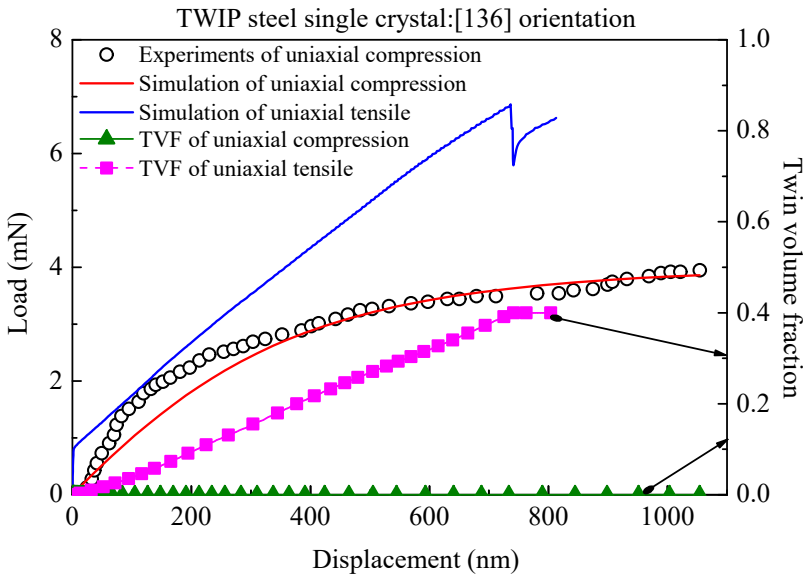

Fig.9. Load-displacement curves for TWIP steel single crystal with the orientation of [136] under uniaxial tensile and compression, and the corresponding evolution of twin volume fraction in deformation.

4.3.2 Effect of twinning and transformation on stress drop for TWIP steel single crystals

In this research, a stress drop, which is similar to the finding of Niewczas et al. (2001) and Yu et al. (2012), is observed during the uniaxial tensile simulation of TWIP steel single crystal with the Euler angle of (10º, 0º, 35º). However, since the presented model considers both the twinning and martensite phase transformation, the capability of the model on representing the stress drop of TWIP steel single crystal is presented and the reason why this phenomenon occurs is given.

In Fig. 10, it is clearly shown that the stress-strain responses using the developed models in this paper have an apparent increase compared with the curve determined by using the model of slip coupling with twinning proposed in previous work (Salem et al., 2005), from which it can be seen that the transformation volume fraction has a great influence on the hardening effect. Furthermore, with the increase of strain increases, both the stress-strain responses

caused by different kinds of models show a steep stress drop. In the presented model, the saturated value of twin volume fraction is considered as a parameter and set to 0.4 based on the experimental results obtained by Renard et al. (Renard et al., 2012). Moreover, the evolution of twin volume fraction of the slip+ twinning+ transformation model does not reach the saturated value when the stress drop appears. So it could be deduced that the stress drop is not caused by the twin induced rotation. Additionally, the Cauchy stress would drop when the transformation induced matrix rotation occurs. Based on the above analysis, the transformation induced rotation would make a contribution to the stress drop for the presented model. It is noted that the stress drop is associated with the decreased slip resistance, which is attributed to the activation of other slip systems.

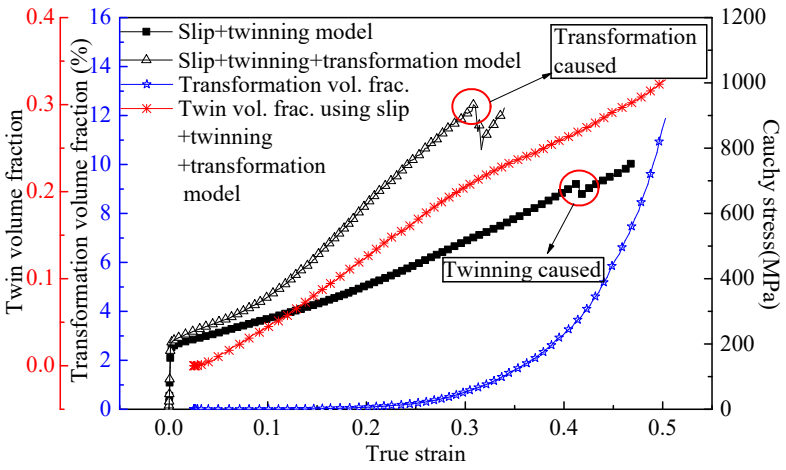

Fig.10. Comparison of the stress-strain response using different models using transformation volume fraction (blue) and twin volume fraction (red) when the Euler angle is (10º, 0º, 35º).

From the curve shown in Fig. 11, the twin volume fraction predicted based on the model of slip coupling with twinning has the valve of 0.4, which means a new orientation occurs. Therefore, the stress drop using the slip coupling with twinning model is caused by twin rotation. In addition, the twinning systems are partly activated and induce plasticity. When the strain reaches about 0.4, however, the twins rotate (the red shadow area) as the twin

volume fraction is up to the saturated value (0.4), which means the twins do not make its effort to intensify the slip resistance.

The model of slip, twinning coupling with transformation shows its ability to capture the crystal deformation behavior, and give a better explanation of steep stress drop during the single crystal plastic deformation process, which proves the reliability of the algorithm.

To provide more powerful evidence for the stress drop of TWIP steel single crystal, the micromechanical behavior of TWIP steel single crystal under particular orientation and proper loading condition needs further study at submicron scale, and the micro evolution of hardening effect may be more helpful to explain the phenomenon of stress drop.

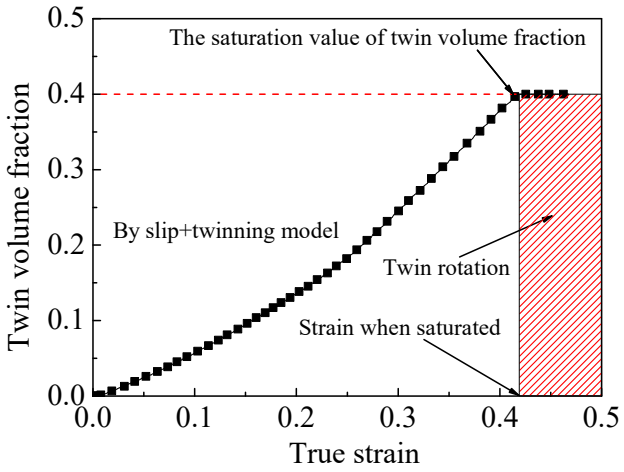

Fig.11. Twin volume fraction with the Euler angle of (10º, 0º, 35º) using the model (slip coupling with twinning). Twin rotation (red shadow) occurs when the twin volume fraction reaches the saturated value of 0.4.

In order to reveal the capability of the model in modeling of the effect of the sequence of twinning and transformation rotation quantitatively on stress-strain response in crystal deformation, a loading process containing different strains of Euler angle (60º, 10º, 0º) at $0.01s^{-1}$ is simulated. It is observed in Fig. 12 (a), with the increase of strain (from 0 to ~0.7), several sharp stress drops appear in the macroscopic response. It is thus proved that these

stress drops are closely associated with the evolution of twin volume fraction and transformation volume fraction. Therefore, it is necessary to determine the sequence of these drops whether they are caused by twinning or transformation. Therefore, this issue could be solved via analysis of the deformation mechanisms under different strains. As described in Section 4.3.1, for the single crystal materials with TWIP effect, the stress drops caused by crystal reorientation appear when the twin volume fraction or transformation volume fraction reaches the saturated value. In Fig. 12 (a), there is no drop in the stress-strain response before the strain of ~0.4. However, the first sharp drop appears when the true strain reaches 0.4. The interpretation of this first stress drop may be referred to the transformation induced rotation and the unsaturated twin volume fraction. Obviously, the two stages (A and B) are divided by this first sharp drop. Since the twin volume fraction does not reach the saturated value at Stages A and B, as shown in Fig. 12 (b), there is no twin induced rotation at both of two stages. However, a secondary sharp stress drop appears when the strain is increased to ~0.5. Corresponding to Fig. 12 (b), the twin volume fraction reaches the saturated value at the strain of ~0.5, i.e., the crystal reorientation caused by the twin induced rotation may lead to the secondary stress drop. Furthermore, when the TWIP single crystal is subjected to plastic deformation to the strain of ~0.7, the sequential deformation mechanisms are determined by different stages: from transformation induced rotation to twin induced rotation.

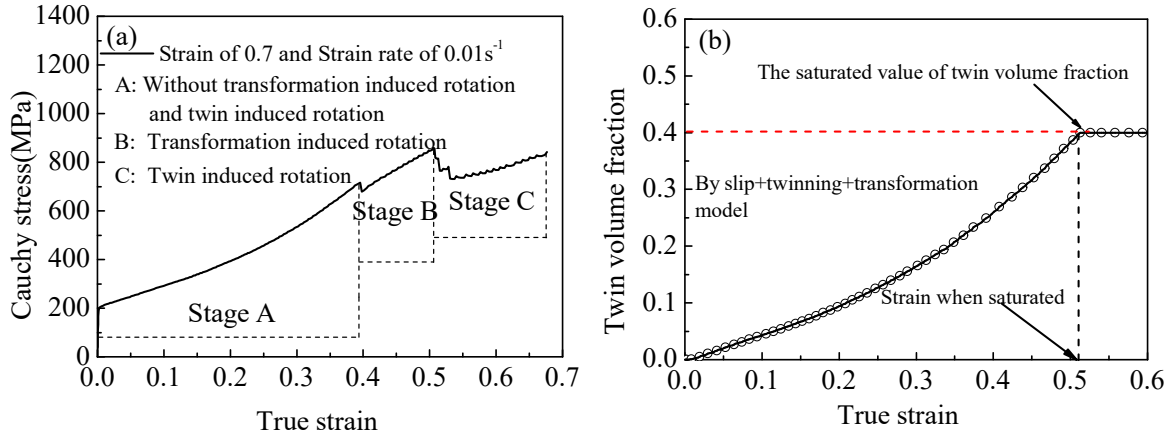

Fig.12. (a) Stress-strain response in uniaxial tensile of TWIP single crystal with Euler angle

(60º, 10º, 0º) (strain of ~0.7 at 0.01s^{-1}); (b) twin volume fraction of Euler angle (60º, 10º, 0º). The red line indicates the saturated value of twin volume fraction.

According to the analysis above, it can be deduced that transformation rotation is prior to the twin rotation with respect to the increasing strain. Therefore, the developed model could model and capture the deformation mechanisms of transformation and twin rotation so that it can reveal the deformation history and process of TWIP single crystal.

5. Conclusions

A constitutive model for modeling of slip, twinning and transformation of TWIP steel crystal based on crystal plasticity was developed in this research to describe the evolution of different mechanisms and the interactions among these micro deformation mechanisms. Based on the developed model and its application in TWIP steel deformation, the following concluding remarks can be drawn:

- Transformation is introduced into the CP framework using the thermodynamic and micromechanical approach, and the threshold of twin volume fraction needs to be given to determine the twin rotation.
- The modified framework is also represented in the formulation of classic rate-dependent constitutive relations so that it is intuitionistic to express the evolution of different deformation mechanisms and their interactions from the point of view of micromechanics.

A fully implicit time-integration scheme based on Newton-Raphson method has been implemented into ABAQUS/Standard using the user material subroutine. The threshold for the twin volume fraction based on the experiments to judge if the twins rotate is introduced. Also, the contribution of the transformation is calculated whether the driving force satisfies the critical value. The accuracy of the modeling has a good agreement with the experimental

results by comparing the simulation results with experiments. In addition, the uniaxial deformation processes of TWIP single crystal are simulated based on the developed model and the algorithms. The following can be concluded:

- Via analysis of twin and martensite + twin volume fraction, the hardening effect of TWIP steel single crystals caused by twinning and transformation could be represented quantitatively and quantitatively by the developed model, which is helpful to predict the trend of stress strain response.
- The stress drop of TWIP single crystal is identified through determination of the saturated value of twin volume fraction, which has an agreement with the experiments in reference. The twin volume fraction can be also used to analyze transformation rotation. The reason why that the transformation causes the stress steep drop is given according to the proposed model.
- The stress-strain response is discussed for determination of the sequence of transformation and twinning rotation quantitatively. The fact that different deformation mechanisms belong to different stages is described using the developed model.

Acknowledgements

Supported by NSAF (No.U1330121), the National Natural Science Foundation of China (No. 51105029), Opening fund of State Key Laboratory of Nonlinear Mechanics (LNM201512), the Beijing Science Foundation of China (No.3112019), and the Doctoral Fund of Ministry of Education of China (No.20100006120013).

References

Abdolvand, H., Daymond, M.R., Mareau, C., 2011. Incorporation of twinning into a crystal plasticity finite element model: Evolution of lattice strains and texture in Zircaloy-2. Int. J. Plast. 27, 1721-1738.

Allain, S., Chateau, J.P., Bouaziz, O., 2004. A physical model of the twinning-induced

plasticity effect in a high manganese austenitic steel. Mater. Sci. Eng. A 387, 143-147.

Asaro, R.J., Needleman, A., 1985. Texture development and strain hardening in rate-dependent polycrystals. Acta Mater. 33, 923-953.

Ball, J.M., James, R.D., 1987. Fine phase mixtures as minimizers of energy. Arch. Ration. Mech. Anal 100, 13-52.

Barbier, D., Favier, V., Bolle, B., 2012. Modeling the deformation textures and microstructural evolutions of a Fe-Mn-C TWIP steel during tensile and shear testing. Mater. Sci. Eng. A 540, 212-225.

Barbier, D., Gey, N., Allain, S., Bozzolo, N., Humbert, M., 2009. Analysis of the tensile behavior of a TWIP steel based on the texture and microstructure evolutions. Mater. Sci. Eng. A 500, 196-206.

Barnett, M.R., Keshavarz, G.Z., Beer, A. 2008, Non-Schmid behavior during secondary twinning in a polycrystalline magnesium alloy. Acta Mater. 56, 5-15.

Beyerlein, I.J., Mara, N.A., Bhattacharyya, D., Alexander, D.J., Necker, C.T., 2011. Texture evolution via combined slip and deformation twinning in rolled silver-copper cast eutectic nanocomposite. Int. J. Plast. 27, 121-146.

Bouaziz, O., 2012. Strain-hardening of twinning-induced plasticity steels. Scripta Mater. 66, 982-985.

Bouaziz, O., Allain, S., Scott, C., 2008. Effect of grain and twin boundaries on the hardening mechanisms of twinning-induced plasticity steels. Scripta Mater. 58, 484-487.

Bouaziz, O., Guelton, N., 2001. Modelling of TWIP effect on work-hardening. Mater. Sci. Eng. A 319, 246-249.

Brown, D.W., Beyerlein, I.J., Sisneros, T.A., Clausen, B., Tome, C.N., 2012. Role of twinning and slip during compressive deformation of beryllium as a function of strain

rate. Int. J. Plast. 29, 120-135.

Capolungo, L., Beyerlein, I.J., Kaschner, G.C., Tomé, C.N., 2009. On the interaction between slip dislocations and twins in HCP Zr. Mater. Sci. Eng. A 513-514, 42-51.

Carvalho Resende, T., Bouvier, S., Abed-Meraim, F., Balan, T., Sablin, S.S., 2013. Dislocation-based model for the prediction of the behavior of b.c.c. materials – Grain size and strain path effects. Int. J. Plast. 47, 29-48.

Chen, P., Ghassemi-Armaki, H., Kumar, S., Bower, A., Bhat, S., Sadagopan, S., 2014. Microscale-calibrated modeling of the deformation response of dual-phase steels. Acta Mater. 65, 133-149.

Cherkaoui, M., Berveiller M., Lemoine. X., 2000. Couplings between plasticity and martensitic phase transformation: overall behavior of polycrystalline TRIP steels. Int. J. Plast. 16, 1215-1241.

Christian, J.W., Mahajan, S., 1995. Deformation twinning. Prog. Mater. Sci. 39, 1–157.

Chung, K., Lee, M.G., Kim, D., Kim, C., Wenner, M.L., Barlat, F., 2005. Spring-back evaluation of automotive sheets based on isotropic-kinematic hardening laws and non-quadratic anisotropic yield functions. Part I: theory and formulation. Int. J. Plast. 21, 861.

Dini, G., Najafizadeh, A., Ueji, R., Monir-Vaghefi, S.M., 2010. Improved tensile properties of partially recrystallized submicron grained TWIP steel. Mater. Lett. 64, 15-18.

Doquet, V., 1993. Twinning and multiaxial cyclic plasticity of a low stacking-fault-energy f.c.c. alloy. Acta Metall. Mater. 41, 2451–2459.

Duhamel, C., Brechet, Y., Champion, Y., 2010. Activation volume and deviation from Cottrell-Stokes law at small grain size. Int. J. Plast. 26, 747-757.

Fischer F.D., Böhm H.J., 2005. On the role of the transformation eigenstrain in the growth or shrinkage of spheroidal isotropic precipitations. Acta Mater. 53, 367-374.

Fischlschweiger, M., Cailletaud, G., Antretter, T., 2012. A mean-field model for transformation induced plasticity including backstress effects for non-proportional loadings. Int. J. Plast. 37, 53-71.

Furnémont, Q., Kempf, M., Jacques, P.J., Göken, M., Delannay, F., 2002. Onthe measurement of thenanohardness of the constitutive phases of TRIP-assisted multiphase steels. Mater. Sci. Eng. A 328, 26–32.

Galindo-Nava, E.I., Rivera-Díaz-del-Castillo, P.E.J., 2014. Thermostastitical modelling of deformation twinning in HCP metals. Int. J. Plast. 55, 25-42.

Gao, C.Y., Zhang, L.C., 2012. Constitutive modelling of plasticity of fcc metals under extremely high strain rates. Int. J. Plast. 32–33, 121-133.

Gebhardt, T., Music, D., Kossmann, D., Ekholm, M., Abrikosov, I.A., Vitos, L., Schneider, J.M., 2011. Elastic properties of fcc Fe–Mn–X (X=Al, Si) alloys studied by theory and experiment. Acta Mater. 59, 3145-3155.

Ghasri-Khouzani, M., McDermid, J.R., 2015. Effect of carbon content on the mechanical properties and microstructural evolution of Fe–22Mn–C steels. Mater. Sci. Eng. A 621, 118-127.

Ghassemi-Armaki, H., Chen, P., Bhat, S., Sadagopan, S., Kumar, S., Bower, A., 2013. Microscale-calibrated modeling of the deformation response of low-carbon martensite. Acta Mater. 61, 3640-3652.

Godet, S., Jiang, L., Luo, A., 2006. Use of Schmid factors to select extension twin variants in extruded magnesium alloy tubes. Scripta Mater. 55, 1055-1058.

Gutierrez-Urrutia, I., Raabe, D., 2012a. Grain size effect on strain hardening in twinning-induced plasticity steels. Scripta Mater. 66, 992-996.

Gutierrez-Urrutia, I., Raabe, D., 2012b. Multistage strain hardening through dislocation substructure and twinning in a high strength and ductile weight-reduced Fe-Mn-Al-C

steel. Acta Mater. 60, 5791-5802.

Hokka, M., Kuokkala, V.T., Curtze, S., Vuoristo, T., Apostol, M., 2006. Characterization of strain rate and temperature dependent mechanical behavior of TWIP steels. J. Phys. IV 134, 1301–1306.

Huang, B.X., Wang, X.D., Rong, Y.H., Wang, L., Jin, L., 2006. Mechanical behavior and martensitic transformation of an Fe-Mn-Si-Al-Nb alloy. Mater. Sci. Eng. A 438, 306-311.

Idrissi, H., Renard, K., Ryelandt, L., Schryvers, D., Jacques, P.J., 2010. On the mechanism of twin formation in Fe-Mn-C TWIP steels. Acta Mater. 58, 2464-2476.

Jiménez, J.A., Frommeyer, G., 2010. Analysis of the microstructure evolution during tensile testing at room temperature of high-manganese austenitic steel. Mater. Charact. 61, 221-226.

Jin, J.E., Lee, Y.K., 2009. Strain hardening behavior of a Fe-18Mn-0.6C-1.5Al TWIP steel. Mater. Sci. Eng. A 527, 157-161.

Kadkhodapour, J., Butz, A., Ziaei-Rad, S., Schmauder, S., 2011. A micro mechanical study on failure initiation of dual phase steels under tension using single crystal plasticity model. Int. J. Plast. 27, 1103-1125.

Kalidindi, S.R., 1998. Incorporation of deformation twinning in crystal plasticity models. J. Mech. Phys. Solids. 46, 267–290.

Kalidindi, S.R., 2001. Modeling anisotropic strain hardening and deformation textures in low stacking fault energy fcc metals. Int. J. Plast. 17, 837–860.

Kalidindi, S.R., 2004. A crystal plasticity framework for deformation twinning. In: Continuum scale simulation of engineering materials. Wiley-VCH; 543–560.

Kalidindi, S.R., Bronkhost, C.A., Anand, L., 1992. Crystallgraphic texture evolution in bulk deformation processing of FCC metals. J. Mech. Phys. Solids. 40, 537-579.

Knezevic, M., Beyerlein, I.J., Brown, D.W., Sisneros, T.A., Tomé, C.N., 2013a. A polycrystal plasticity model for predicting mechanical response and texture evolution during strain-path changes: Application to beryllium. Int. J. Plast. 49, 185-198.

Knezevic, M., Beyerlein, I.J., Lovato, M.L., Tomé, C.N., Richards, A.W., McCabe, R.J., 2014. A strain-rate and temperature dependent constitutive model for BCC metals incorporating non-Schmid effects: Application to tantalum–tungsten alloys. Int. J. Plast. 62, 93-104.

Knezevic, M., McCabe, R.J., Tome, C.N., Lebensohn, R.A., Chen, S.R., Cady, C.M., Gray, G.T., Mihaila, B., 2013b. Modeling mechanical response and texture evolution of alpha-uranium as a function of strain rate and temperature using polycrystal plasticity. Int. J. Plast. 43, 70-84.

Koyama, M., Sawaguchi, T., Lee, T., Lee, C.S., Tsuzaki, K., 2011. Work hardening associated with ε-martensitic transformation, deformation twinning and dynamic strain aging in Fe–17Mn–0.6C and Fe–17Mn–0.8C TWIP steels. Mater. Sci. Eng. A 528, 7310-7316.

Lee, W., Chung, K.-H., Kim, D., Kim, J., Kim, C., Okamoto, K., Wagoner, R.H., Chung, K., 2009. Experimental and numerical study on formability of friction stir welded TWB sheets based on hemispherical dome stretch tests. Int. J. Plast. 25, 1626-1654.

Lee, M.-G., Kim, S.-J., Han, H.N., 2010. Crystal plasticity finite element modeling of mechanically induced martensitic transformation (MIMT) in metastable austenite. Int. J. Plast. 26, 688-710.

Levitas, V.I., 2002. Critical thought experiment to choose the driving force for interface propagation in inelastic materials. Int. J. Plast. 18, 1499-1525.

Levitas, V.I., Ozsoy, I.B., 2009. Micromechanical modeling of stress-induced phase transformations. Part 1. Thermodynamics and kinetics of coupled interface

propagation and reorientation. Int. J. Plast. 25, 239-280.

Li, H.W., Yang, H., Sun, Z.C., 2008. A robust integration algorithm for implementing rate dependent crystal plasticity into explicit finite element method. Int. J. Plast. 24, 267-288.

Li, M., Lou, X.Y., Kim, J.H., Wagoner, R.H., 2010. An efficient constitutive model for room-temperature, low-rate plasticity of annealed Mg AZ31B sheet. Int. J. Plast. 26, 820-858.

Liang, X., McDermid, J.R., Bouaziz, O., Wang, X., Embury, J.D., Zurob, H.S., 2009. Microstructural evolution and strain hardening of Fe-24Mn and Fe-30Mn alloys during tensile deformation. Acta Mater. 57, 3978-3988.

Manchiraju, S., Anderson, P.M., 2010. Coupling between martensitic phase transformations and plasticity: A microstructure-based finite element model. Int. J. Plast. 26, 1508-1526.

Marin, E.B., Dawson, P.R., 1998. On modeling the elasto-viscoplastic response of metals using polycrystal plasticity. Comput. Meth. Appl. Mech. Eng. 165, 1-21.

Mi, Z.L., Tang, D., Yan, L., Guo, J., 2005. High-strength and high-plasticity TWIP steel for modern vehicle. J. Mater. Sci. Technol. 21, 451-454.

Mohr, D., Dunand, M., Kim, K.-H., 2010. Evaluation of associated and non-associated quadratic plasticity models for advanced high strength steel sheets under multi-axial loading. Int.J.Plast. 26, 939-956.

Niewczas, M., Basinski, Z.S., Basinski, S.J., Embury, J.D., 2001a. Deformation of copper single crystals to large strains at 4.2K. Philo. Mag. A 81, 1121-1142.

Niezgoda, S.R., Kanjarla, A.K., Beyerlein, I.J., Tomé, C.N., 2014. Stochastic modeling of twin nucleation in polycrystals: An application in hexagonal close-packed metals. Int.J.Plast. 56, 119-138.

Oberson, P.G., Ankem, S., 2009. The effect of time-dependent twinning on low temperature (< 0.25*T-m) creep of an alpha-titanium alloy. Int. J.P last. 25, 881-900.

Oppedal, A.L., El Kadiri, H., Tomé, C.N., Kaschner, G.C., Vogel, S.C., Baird, J.C., Horstemeyer, M.F., 2012. Effect of dislocation transmutation on modeling hardening mechanisms by twinning in magnesium. Int. J. Plast. 30-31, 41-61.

Perlade, A., Bouaziz, O., Furnemont, Q., 2003. A physically based model. for TRIP-aided carbon steels behaviour. Mater. Sci. Eng. A 356, 145-152.

Piao, K., Lee, J.K., Kim, J.H., Kim, H.Y., Chung, K., Barlat, F., Wagoner, R.H., 2012. A sheet tension/compression test for elevated temperature. Int. J. Plast. 38, 27-46.

Pierce, D., Asaro, R.J., Needleman, A., 1982. An analysis of nonuniform and localized deformation in ductile single crystals. Acta Mater. 30, 1087.

Pierce, D.T., Nowag, K., Montagne, A., Jiménez, J.A., Wittig, J.E., Ghisleni, R., 2013. Single crystal elastic constants of high-manganese transformation- and twinning-induced plasticity steels determined by a new method utilizing nanoindentation. Mater.Sci.Eng.A 578, 134-139.

Renard, K., Jacques, P. J., 2012. On the relationship between work hardening and twinning rate in TWIP steels. Mater. Sci. Eng. A 542, 8-14.

Sabet, M., Zarei-Hanzaki, A., Khoddam, S., 2009. Dynamic Restoration Processes in High-Mn TWIP Steels. J. Eng. Mater. Technol. 131.

Saleh, A.A., Pereloma, E.V., Clausen, B., Brown, D.W., Tomé, C.N., Gazder, A.A., 2013. On the evolution and modelling of lattice strains during the cyclic loading of TWIP steel. Acta Mater. 61, 5247-5262.

Salem, A.A., Kalidindi, S.R., Semiatin, S.L., 2005. Strain hardening due to deformation twinning in alpha-titanium: Constitutive relations and crystal-plasticity modeling. Acta Mater. 53, 3495-3502.

Sevillano, J.G., 2009. An alternative model for the strain hardening of FCC alloys that twin, validated for twinning-induced plasticity steel. Scripta Mater. 60, 336-339.

Shiekhelsouk, M.N., Favier, V., Inal, K., Cherkaoui, M., 2009. Modelling the behaviour of polycrystalline austenitic steel with twinning-induced plasticity effect. Int. J. Plast. 25, 105-133.

Shin, J.H., Kim, S.H., Ha, T.K., Oh, K.H., Choi, I.S., Han, H.N., 2013. Nanoindentation study for deformation twinning of magnesium single crystal. Scripta Mater. 68, 483-486.

Srivastava, A., Ghassemi-Armaki, H., Sung, H., Chen, P., Kumar, S., Bower, A.F., 2015. Micromechanics of plastic deformation and phase transformation in a three-phase TRIP-assisted advanced high strength steel: Experiments and modeling. J. Mech. Phys. Solids 78, 46-69.

Staroselsky, A., Anand, L., 2003. A constitutive model for hcp materials deforming by slip and twinning. Int. J. Plast. 19, 1843-1864.

Suiker, A.S.J., Turteltaub, S., 2005. Computational modelling of plasticity induced by martensitic phase transformations. Int. J. Numer. Methods Eng. 63, 1655-1693.

Sun, C.Y., Huang J., Guo, N., Yang, J., 2014. A physical constitutive model based on dislocation denstity of Fe-22Mn-0.6C TWIP steel. Acta Metall. Sin.50, 1115-1122.

Sun, C.Y., Huang J., Guo, N., Yang, J., Wang B., 2015. Sensitivity analysis of hardening parameters in the crystal plasticity model exhibiting deformation twinning. Chinese J. Eng., accepted.

Sun, L., Wagoner, R.H., 2013. Proportional and non-proportional hardening behavior of dual-phase steels. Int. J. Plast. 45, 174-187.

Sun, W., Chaikof, E.L., Levenston, M.E., 2008. Numerical approximation of tangent moduli for finite element implementations of nonlinear hyperelastic material models. J. Biomech.

Eng. 130, 061003.

Sung, J.H., Kim, J.H., Wagoner, R.H., 2010. A plastic constitutive equation incorporating strain, strain-rate, and temperature. Int. J. Plast. 26, 1746-1771.

Szyndler, J., Madej, Ł., 2015. Numerical analysis of the influence of number of grains, FE mesh density and friction coefficient on representativeness aspects of the polycrystalline digital material representation-Plane strain deformation case study. Comp. Mater. Sci. 96, 200-213.

Tjahjanto, D.D., Turteltaub, S., Suiker, A.S.J., 2008a. Crystallographically based model for transformation-induced plasticity in multiphase carbon steels. Continuum Mech. Thermodyn. 19, 399-422.

Tjahjanto, D.D., Turteltaub, S., Suiker, A.S.J., van der Zwaag, S., 2008b. Transformation-induced plasticity in multiphase steels subjected to thermomechanical loading. Philos. Mag. 88, 3369-3387.

Turteltaub, S., Suiker, A.S.J., 2005. Transformation-induced plasticity in ferrous alloys. J. Mech. Phys. Solids 53, 1747-1788.

Vercammen, S., Blanpain, B., De Cooman, B.C., Wollants, P., 2004. Cold rolling behaviour of an austenitic, Fe-30Mn-3Al-3Si TWIP-steel: the importance of deformation twinning. Acta Mater. 52, 2005-2012.

Wang, H., Wu, P.D., Wang, J., Tomé, C.N., 2013. A crystal plasticity model for hexagonal close packed (HCP) crystals including twinning and de-twinning mechanisms. Int. J. Plast. 49, 36-52.

Wu, P.D., Guo, X.Q., Qiao, H., Lloyd, D.J., 2015. A constitutive model of twin nucleation, propagation and growth in magnesium crystals. Mater.Sci.Eng.A 625, 140-145.

Wu, S.Z., Yen, H.W., Huang, M.X., Ngan, A.H.W., 2012. Deformation twinning in submicron and micron pillars of twinning-induced plasticity steel. Scripta Mater. 67,

641-644.

Wu, X., Kalidindi, S., Necker, C., Salem, A., 2007. Prediction of crystallographic texture evolution and anisotropic stress–strain curves during large plastic strains in high purity α-titanium using a Taylor-type crystal plasticity model. Acta Mater. 55, 423-432.

Wu, Z.Q., Tang, Z.Y., Li, H.Y., Zhang, H.D., 2012. Effect of strain rate on microstructure evolution and mechanical behavior of a low C high Mn TRIP/TWIP steels. Acta Metall. 48, 593-600.

Yang, H.K., Zhang, Z.J., Zhang, Z.F., 2013. Comparison of work hardening and deformation twinning evolution in Fe-22Mn-0.6C (1.5Al) twinning-induced plasticity steels. Scripta Mater. 68, 992-995.

Yang, P., Lu, F.Y., Meng, L., Cui, F.E., 2010. Crystallographic behaviors of compressed high manganese TRIP/TWIP steels analyzed by EBSD techniques. Acta Metall. 6, 657-665.

Yang, P., Xie, Q., Meng, L., Ding, H., Tang, Z., 2006. Dependence of deformation twinning on grain orientation in a high manganese steel. Scripta Mater. 55, 629-631.

Yu, Q., Qi, L., Chen, K., Mishra, R.K., Li, J., Minor, A.M., 2012. The nanostructured origin of deformation twinning. Nano Lett. 12, 887-892.

Zambaldi, C., Zehnder, C., Raabe, D., 2015. Orientation dependent deformation by slip and twinning in magnesium during single crystal indentation. Acta Mater. 91, 267-288.

Zeng, W., Larsen, J.M., Liu, G.R., 2015. Smoothing technique based crystal plasticity finite element modeling of crystalline materials. Int. J. Plast. 65, 250-268.

Zhang, H., Huang, G., Fan, J., Roven, H.J., Xu, B., Dong, H., 2014. Deep drawability and drawing behaviour of AZ31 alloy sheets with different initial texture. J. Alloy. Compd. 615, 302-310.

Figure captions

Fig.1. Schematic of different micro-deformation mechanisms. (a) Production of slip deformation by a homogeneous shear. Atoms move along the slip plane under the shear stress τ, and N stands for the normal to the slip plane. (b) Schematic of twin shear deformation. λ_T denotes the twinning shear and the dashed line indicates the average shear of the material volume. (c) The parent phase (red dashed line) translates to martensite (black solid line) under the effect of shear deformation; the **m** and **n** indicate the transformation direction and the normal to habit plane, respectively. (d) Crystal rotation during the process of uniaxial tensile; the α and γ denote the amount of shear with respect to the status before rotation and after rotation, respectively.

Fig.2. The schematic representation of the classic decomposition of deformation gradient **F**, which is divided into the elastic and plastic parts.

Fig.3. The improvement of classic intermediate configuration into five configurations is illustrated and the corresponding decomposition of deformation gradient **F** into the elastic, plastic and transformation parts is described.

Fig.4. The flow chart of numerical algorithm into implicit FEM.

Fig.5. Comparison of (a) stress-strain responses and (b) work hardening rate from simulation with those from experiments performed at different temperatures (Koyama et al., 2011).

Fig.6. The effects of different Euler angles (10º, 0º, 35º) and (60º, 10º, 0º) on hardening for TWIP single crystal at the strain rate $0.001s^{-1}$ when the true strain reaches 0.4 and 0.48 respectively. And the strain hardening rate of Euler angle (10º, 0º, 35º) is given particularly.

Fig.7. Sum of martensite and twin volume fractions versus strain for the TWIP steel single crystal with the Euler angle (10º, 0º, 35º), including its evolution of twin volume fraction against experimental results.

Fig.8. Evolution of macroscopic response for copper single crystals with [001] and [541]

orientations under uniaxial tensile condition, including their twin volume fraction.

Fig.9. Load-displacement curves for TWIP steel single crystal with [136] orientation under uniaxial tensile and compression, together with the corresponding evolution of twin volume fraction.

Fig.10. Comparison of the stress-strain response using different models using transformation volume fraction (blue) and twin volume fraction (red) when the Euler angle is (10º, 0º, 35º).

Fig.11. Twin volume fraction with the Euler angle of (10º, 0º, 35º) using the model (slip coupling with twinning). Twin rotation (red shadow) occurs when the twin volume fraction reaches the saturated value of 0.4.

Fig.12. (a) Stress-strain response in uniaxial tensile of TWIP single crystal with Euler angle (60º, 10º, 0º) (strain of ~0.7 at $0.01s^{-1}$); (b) twin volume fraction of Euler angle (60º, 10º, 0º). The red line indicates the saturated value of twin volume fraction.

Table captions

Table 1. Reference for different factors on deformation twinning.

Table 2. Material parameters in the constitutive relations calibrated for TWIP steel.

Box captions

Box 1. Constitutive model coupling slip-twinning-transformation of TWIP steel.

Box 2. Summary of the stress update algorithm for the rate-dependent constitutive model.